

## A model for human ventricular tissue

K. H. W. J. ten Tusscher,<sup>1</sup> D. Noble,<sup>2</sup> P. J. Noble,<sup>2</sup> and A. V. Panfilov<sup>1,3</sup>

<sup>1</sup>Department of Theoretical Biology, Utrecht University, 3584 CH Utrecht, The Netherlands;

and <sup>2</sup>University Laboratory of Physiology, University of Oxford, Oxford OX1 3PT; and

<sup>3</sup>Division of Mathematics, University of Dundee, Dundee DD1 4HN, United Kingdom

Submitted 9 August 2003; accepted in final form 2 December 2003

**Ten Tusscher, K. H. W. J., D. Noble, P. J. Noble, and A. V. Panfilov.** A model for human ventricular tissue. *Am J Physiol Heart Circ Physiol* 286: H1573–H1589, 2004. First published December 4, 2003; 10.1152/ajpheart.00794.2003.—The experimental and clinical possibilities for studying cardiac arrhythmias in human ventricular myocardium are very limited. Therefore, the use of alternative methods such as computer simulations is of great importance. In this article we introduce a mathematical model of the action potential of human ventricular cells that, while including a high level of electrophysiological detail, is computationally cost-effective enough to be applied in large-scale spatial simulations for the study of reentrant arrhythmias. The model is based on recent experimental data on most of the major ionic currents: the fast sodium, L-type calcium, transient outward, rapid and slow delayed rectifier, and inward rectifier currents. The model includes a basic calcium dynamics, allowing for the realistic modeling of calcium transients, calcium current inactivation, and the contraction staircase. We are able to reproduce human epicardial, endocardial, and M cell action potentials and show that differences can be explained by differences in the transient outward and slow delayed rectifier currents. Our model reproduces the experimentally observed data on action potential duration restitution, which is an important characteristic for reentrant arrhythmias. The conduction velocity restitution of our model is broader than in other models and agrees better with available data. Finally, we model the dynamics of spiral wave rotation in a two-dimensional sheet of human ventricular tissue and show that the spiral wave follows a complex meandering pattern and has a period of 265 ms. We conclude that the proposed model reproduces a variety of electrophysiological behaviors and provides a basis for studies of reentrant arrhythmias in human ventricular tissue.

reentrant arrhythmias; human ventricular myocytes; restitution properties; spiral waves; computer simulation

CARDIAC ARRHYTHMIAS and sudden cardiac death are among the most common causes of death in the industrialized world. Despite decades of research their causes are still poorly understood. Theoretical studies into the mechanisms of cardiac arrhythmias form a well-established area of research. One of the most important applications of these theoretical studies is the simulation of the human heart, which is important for a number of reasons. First, the possibilities for doing experimental and clinical studies involving human hearts are very limited. Second, animal hearts used for experimental studies may differ significantly from human hearts [heart size, heart rate, action potential (AP) shape, duration, and restitution, vulnerability to arrhythmias, etc.]. Finally, cardiac arrhythmias, especially those occurring in the ventricles, are three-dimensional phenomena whereas experimental observations are still largely

constrained to surface recordings. Computer simulations of arrhythmias in the human heart can overcome some of these problems.

To perform simulation studies of reentrant arrhythmias in human ventricles we need a mathematical model that on the one hand reproduces detailed properties of single human ventricular cells, such as the major ionic currents, calcium transients, and AP duration (APD) restitution (APDR), and important properties of wave propagation in human ventricular tissue, such as conduction velocity (CV) restitution (CVR). On the other hand, it should be computationally efficient enough to be applied in the large-scale spatial simulations needed to study reentrant arrhythmias.

Currently, the only existing model for human ventricular cells is the Priebe-Beuckelman (PB) model and the reduced version of this model constructed by Bernus et al. (3, 51). The PB model is largely based on the phase 2 Luo-Rudy (LR) model for guinea pig ventricular cells (38). Although the model incorporates some data on human cardiac cells and successfully reproduces basic properties of APs of normal and failing human ventricular cells, it has several limitations. First, several major ionic currents are still largely based on animal data, and second, the APD is 360 ms, which is much longer than the values typically recorded in tissue experiments (~270 ms; Ref. 36). The aim of this work was to formulate a new model for human ventricular cells that is based on recent experimental data and that is efficient for large-scale spatial simulations of reentrant phenomena.

We formulated a model in which most major ionic currents [fast Na<sup>+</sup> current ( $I_{Na}$ ), L-type Ca<sup>2+</sup> current ( $I_{CaL}$ ), transient outward current ( $I_{to}$ ), rapid delayed rectifier current ( $I_{Kr}$ ), slow delayed rectifier current ( $I_{Ks}$ ), and inward rectifier K<sup>+</sup> current ( $I_{K1}$ )] are based on recent experimental data. The model includes a simple calcium dynamics that reproduces realistic calcium transients and a positive human contraction staircase and allows us to realistically model calcium-dominated  $I_{CaL}$  inactivation, while at the same time maintaining a low computational load.

The model fits experimentally measured APDR properties of human myocardium (42). In addition, the CVR properties of our model agree better with experimental data—which are currently only available for dog and guinea pig (6, 19)—than those of existing ionic models. Both APD and CV restitution are very important properties for the occurrence and stability of reentrant arrhythmias (6, 17, 31, 52, 67). Our model is able to reproduce the different AP shapes corresponding to the endo-, epi-, and midmyocardial regions of the ventricles and their

Address for reprint requests and other correspondence: K. H. W. J. ten Tusscher, Utrecht Univ., Dept. of Theoretical Biology, Padualaan 8, 3584 CH Utrecht, The Netherlands (E-mail: khwtjuss@hotmail.com).

The costs of publication of this article were defrayed in part by the payment of page charges. The article must therefore be hereby marked “advertisement” in accordance with 18 U.S.C. Section 1734 solely to indicate this fact.

different rate dependencies (9, 10, 36). Finally, we model spiral wave dynamics in a two-dimensional (2D) sheet of human ventricular tissue and study the dynamics of its rotation, the ECG manifestation of the spiral wave, and membrane potential recordings during spiral wave rotation. In conclusion, we propose a new model for human ventricular tissue that is feasible for large-scale spatial computations of reentrant sources of cardiac arrhythmias.

## MATERIALS AND METHODS

### General

The cell membrane is modeled as a capacitor connected in parallel with variable resistances and batteries representing the different ionic currents and pumps. The electrophysiological behavior of a single cell can hence be described with the following differential equation (23)

$$\frac{dV}{dt} = -\frac{I_{\text{ion}} + I_{\text{stim}}}{C_m} \quad (1)$$

where  $V$  is voltage,  $t$  is time,  $I_{\text{ion}}$  is the sum of all transmembrane ionic currents,  $I_{\text{stim}}$  is the externally applied stimulus current, and  $C_m$  is cell capacitance per unit surface area.

Similarly, ignoring the discrete character of microscopic cardiac cell structure, a 2D sheet of cardiac cells can be modeled as a continuous system with the following partial differential equation (23)

$$\frac{\partial V}{\partial t} = -\frac{I_{\text{ion}} + I_{\text{stim}}}{C_m} + \frac{1}{\rho_x S_x C_m} \frac{\partial^2 V}{\partial x^2} + \frac{1}{\rho_y S_y C_m} \frac{\partial^2 V}{\partial y^2} \quad (2)$$

where  $\rho_x$  and  $\rho_y$  are the cellular resistivity in the  $x$  and  $y$  directions,  $S_x$  and  $S_y$  are the surface-to-volume ratio in the  $x$  and  $y$  directions, and  $I_{\text{ion}}$  is the sum of all transmembrane ionic currents given by the following equation

$$I_{\text{ion}} = I_{\text{Na}} + I_{\text{K1}} + I_{\text{to}} + I_{\text{Kr}} + I_{\text{Ks}} + I_{\text{CaL}} + I_{\text{NaCa}} + I_{\text{NaK}} + I_{\text{pCa}} + I_{\text{pK}} + I_{\text{bCa}} + I_{\text{bNa}} \quad (3)$$

where  $I_{\text{NaCa}}$  is  $\text{Na}^+/\text{Ca}^{2+}$  exchanger current,  $I_{\text{NaK}}$  is  $\text{Na}^+/\text{K}^+$  pump current,  $I_{\text{pCa}}$  and  $I_{\text{pK}}$  are plateau  $\text{Ca}^{2+}$  and  $\text{K}^+$  currents, and  $I_{\text{bCa}}$  and  $I_{\text{bK}}$  are background  $\text{Ca}^{2+}$  and  $\text{K}^+$  currents.

Physical units used in our model are as follows: time ( $t$ ) in milliseconds, voltage ( $V$ ) in millivolts, current densities ( $I_x$ ) in picoamperes per picofarad, conductances ( $G_x$ ) in nanosiemens per picofarad, and intracellular and extracellular ionic concentrations ( $X_i$ ,  $X_o$ ) in millimoles per liter. The equations for the ionic currents are specified in *Membrane Currents*.

For one-dimensional (1D) computations cell capacitance per unit surface area is taken as  $C_m = 2.0 \mu\text{F}/\text{cm}^2$  and surface-to-volume ratio is set to  $S = 0.2 \mu\text{m}^{-1}$ , following Bernus et al. (3). To obtain a maximum planar conduction velocity (CV) of 70 cm/s, the velocity found for conductance along the fiber direction in human myocardium by Taggart et al. (61), a cellular resistivity  $\rho = 162 \Omega\text{cm}$  was required. This is comparable to the  $\rho = 180 \Omega\text{cm}$  used by Bernus et al. (3) and the  $\rho = 181 \Omega\text{cm}$  used by Jongsma and Wilders (29), and it results in a “diffusion” coefficient  $D = 1/(\rho S C_m)$  of  $0.00154 \text{ cm}^2/\text{ms}$ . Because in 2D we did not intend to study the effects of anisotropy, we use the same values for  $\rho_x$  and  $\rho_y$  and for  $S_x$  and  $S_y$ . Parameters of the model are given in Table 1.

For 1D and 2D computations, the forward Euler method was used to integrate Eq. 1. A space step of  $\Delta x = 0.1\text{--}0.2 \text{ mm}$  and a time step of  $\Delta t = 0.01\text{--}0.02 \text{ ms}$  were used. To integrate the Hodgkin-Huxley-type equations for the gating variables of the various time-dependent currents ( $m$ ,  $h$ , and  $j$  for  $I_{\text{Na}}$ ,  $r$  and  $s$  for  $I_{\text{to}}$ ,  $x_{r1}$  and  $x_{r2}$  for  $I_{\text{Kr}}$ ,  $x_s$  for  $I_{\text{Ks}}$ ,  $d$ ,  $f$ , and  $f_{\text{Ca}}$  for  $I_{\text{CaL}}$ , and  $g$  for  $I_{\text{rel}}$ ) the Rush and Larsen scheme (54) was used.

Table 1. *Model parameters*

Parameter	Definition	Value
$R$	Gas constant	$8.3143 \text{ J}\cdot\text{K}^{-1}\cdot\text{mol}^{-1}$
$T$	Temperature	310 K
$F$	Faraday constant	$96.4867 \text{ C}/\text{mmol}$
$C_m$	Cell capacitance per unit surface area	$2 \mu\text{F}/\text{cm}^2$
$S$	Surface-to-volume ratio	$0.2 \mu\text{m}^{-1}$
$\rho$	Cellular resistivity	$162 \Omega\cdot\text{cm}$
$V_C$	Cytoplasmic volume	$16,404 \mu\text{m}^3$
$V_{\text{SR}}$	Sarcoplasmic reticulum volume	$1,094 \mu\text{m}^3$
$K_O$	Extracellular $\text{K}^+$ concentration	5.4 mM
$\text{Na}_O$	Extracellular $\text{Na}^+$ concentration	140 mM
$\text{Ca}_O$	Extracellular $\text{Ca}^{2+}$ concentration	2 mM
$G_{\text{Na}}$	Maximal $I_{\text{Na}}$ conductance	$14.838 \text{ nS}/\text{pF}$
$G_{\text{K1}}$	Maximal $I_{\text{K1}}$ conductance	$5.405 \text{ nS}/\text{pF}$
$G_{\text{to, epi, M}}$	Maximal epicardial $I_{\text{to}}$ conductance	$0.294 \text{ nS}/\text{pF}$
$G_{\text{to, endo}}$	Maximal endocardial $I_{\text{to}}$ conductance	$0.073 \text{ nS}/\text{pF}$
$G_{\text{Kr}}$	Maximal $I_{\text{Kr}}$ conductance	$0.096 \text{ nS}/\text{pF}$
$G_{\text{Ks, epi, endo}}$	Maximal epi- and endocardial $I_{\text{Ks}}$ conductance	$0.245 \text{ nS}/\text{pF}$
$G_{\text{Ks, M}}$	Maximal M cell $I_{\text{Ks}}$ conductance	$0.062 \text{ nS}/\text{pF}$
$P_{\text{KNa}}$	Relative $I_{\text{Ks}}$ permeability to $\text{Na}^+$	0.03
$G_{\text{CaL}}$	Maximal $I_{\text{CaL}}$ conductance	$1.75^{-4} \text{ cm}^3\cdot\mu\text{F}^{-1}\cdot\text{s}^{-1}$
$g_{\text{NaCa}}$	Maximal $I_{\text{NaCa}}$	$1,000 \text{ pA}/\text{pF}$
$\gamma$	Voltage dependence parameter of $I_{\text{NaCa}}$	0.35
$K_{\text{mCa}}$	$\text{Ca}_i$ half-saturation constant for $I_{\text{NaCa}}$	1.38 mM
$K_{\text{mNa}}$	$\text{Na}_i$ half-saturation constant for $I_{\text{NaCa}}$	87.5 mM
$k_{\text{sat}}$	Saturation factor for $I_{\text{NaCa}}$	0.1
$\alpha$	Factor enhancing outward nature of $I_{\text{NaCa}}$	2.5
$P_{\text{NaK}}$	Maximal $I_{\text{NaK}}$	$1.362 \text{ pA}/\text{pF}$
$K_{\text{mK}}$	$\text{K}_O$ half-saturation constant of $I_{\text{NaK}}$	1 mM
$K_{\text{mNa}}$	$\text{Na}_i$ half-saturation constant of $I_{\text{NaK}}$	40 mM
$G_{\text{pK}}$	Maximal $I_{\text{pK}}$ conductance	$0.0146 \text{ nS}/\text{pF}$
$G_{\text{pCa}}$	Maximal $I_{\text{pCa}}$ conductance	$0.025 \text{ nS}/\text{pF}$
$K_{\text{pCa}}$	$\text{Ca}_i$ half-saturation constant of $I_{\text{pCa}}$	0.0005 mM
$G_{\text{bNa}}$	Maximal $I_{\text{bNa}}$ conductance	$0.00029 \text{ nS}/\text{pF}$
$G_{\text{bCa}}$	Maximal $I_{\text{bCa}}$ conductance	$0.000592 \text{ nS}/\text{pF}$
$V_{\text{maxup}}$	Maximal $I_{\text{up}}$	$0.000425 \text{ mM}/\text{ms}$
$K_{\text{up}}$	Half-saturation constant of $I_{\text{up}}$	0.00025 mM
$a_{\text{rel}}$	Maximal $\text{Ca}_{\text{SR}}$ -dependent $I_{\text{rel}}$	16.464 mM/s
$b_{\text{rel}}$	$\text{Ca}_{\text{SR}}$ half-saturation constant of $I_{\text{rel}}$	0.25 mM
$c_{\text{rel}}$	Maximal $\text{Ca}_{\text{SR}}$ -independent $I_{\text{rel}}$	8.232 mM/s
$V_{\text{leak}}$	Maximal $I_{\text{leak}}$	$0.00008 \text{ ms}^{-1}$
$\text{Buf}_c$	Total cytoplasmic buffer concentration	0.15 mM
$K_{\text{bufc}}$	$\text{Ca}_i$ half-saturation constant for cytoplasmic buffer	0.001 mM
$\text{Buf}_{\text{sr}}$	Total sarcoplasmic buffer concentration	10 mM
$K_{\text{bufsr}}$	$\text{Ca}_{\text{SR}}$ half-saturation constant for sarcoplasmic buffer	0.3 mM

We test the accuracy of our numerical simulations in a cable of cells by varying both the time and space steps of integration. The results of these tests are shown in Table 2. From Table 2 it follows that, with a  $\Delta x = 0.2 \text{ mm}$ , decreasing  $\Delta t$  from 0.02 to 0.0025 ms leads to a 3.7% increase in CV. Similarly, with  $\Delta t = 0.02 \text{ ms}$ , decreasing  $\Delta x$  from 0.2 to 0.1 mm leads to an increase in CV of 4.6%. The changes in CV occurring for changes in space and time integration steps are similar to those occurring in other models (see, for example, Ref. 52). The time and space steps used in most computations are  $\Delta t = 0.02 \text{ ms}$  and  $\Delta x = 0.2 \text{ mm}$ , similar to values used in other studies (3, 6, 52, 69). Major conclusions of our model were tested for smaller space and time steps; the results were only slightly different.

Action potential duration (APD) is defined as action potential duration at 90% repolarization ( $\text{APD}_{90}$ ). Two different protocols were used to determine APD restitution (APDR). The S1-S2 restitution protocol, typically used in experiments, consists of 10 S1 stimuli

Table 2. Numerical accuracy of conduction velocity for different  $\Delta t$  and  $\Delta x$

$\Delta x$ , cm	Conduction Velocity, cm/s			
	$\Delta t = 0.0025$ ms	$\Delta t = 0.005$ ms	$\Delta t = 0.01$ ms	$\Delta t = 0.02$ ms
0.010	75.4	75.0	74.2	72.5
0.015	74.4	73.8	73.0	71.5
0.020	71.9	71.5	70.8	69.3
0.030	67.8	67.4	66.8	65.7
0.040	63.2	63.0	62.6	61.7

applied at a frequency of 1 Hz and a strength of two times the threshold value, followed by a S2 extrastimulus delivered at some diastolic interval (DI) after the AP generated by the last S1 stimulus. The APDR curve is generated by decreasing DI and plotting APD generated by the S2 stimulus against DI. The second restitution protocol is called the dynamic restitution protocol. It was first proposed by Koller et al. (32) as being a more relevant determinant of spiral wave stability than S1-S2 restitution. The protocol consists of a series of stimuli at a certain cycle length until a steady-state APD is reached; after that, cycle length is decreased. The APDR curve is obtained by plotting steady-state APDs against steady-state DIs. CV restitution (CVR) was simulated in a linear strand of 400 cells by pacing it at one end at various frequencies and measuring CV in the middle of the cable.

Spiral waves were initiated in 2D sheets of ventricular tissue with the S1-S2 protocol. We first applied a single S1 stimulus along the entire length of one side of the tissue, producing a planar wave front propagating in one direction. When the refractory tail of this wave crossed the middle of the medium, a second S2 stimulus was applied in the middle of the medium, parallel to the S1 wave front but only over three-quarters of the length of the medium. This produces a second wave front with a free end around which it curls, thus producing a spiral wave. Stimulus currents lasted for 2 (S1) and 5 (S2) ms and were two times diastolic threshold. The trajectory of the spiral tip was traced with an algorithm suggested by Fenton and Karma (16). It is based on the idea that the spiral tip is defined as the point where excitation wave front and repolarization wave back meet. This point can be found as the intersection point of an isopotential line (in our case,  $-35$  mV) and the  $dV/dt = 0$  line.

Electrograms of spiral wave activity were simulated in 2D by calculating the dipole source density of the membrane potential  $V$  in each element, assuming an infinite volume conductor (50). The electrogram was recorded with a single electrode located 10 cm above the center of the sheet of tissue.

All simulations were written in C<sup>++</sup>. Single-cell and cable simulations were run on a PC Intel Pentium III 800-MHz CPU; 2D simulations were run on 32 500-MHz processors of a SGI Origin 3800 shared-memory machine, using OpenMP for parallelization (Source code available at <http://www.binf.bio.uu.nl/khwjtuss/HVM>).

A description of the membrane currents of the model and the experimental data on which they are based is given in *Membrane Currents*. For most currents a comparison is made with the formulations used in existing models for human ventricular myocytes by Priebe and Beuckelmann (51)—for the rest of the text referred to as the PB model—and for human atrial myocytes by Courtemanche and coworkers (8)—for the rest of the text referred to as the CRN model. For the fast  $\text{Na}^{2+}$  current a comparison is made to the widely used  $I_{\text{Na}}$  formulation first used in phase 1 of the Luo-Rudy (LR) model (37) that is used in both the PB and CRN model. The LR  $I_{\text{Na}}$  formulation is largely based on the  $I_{\text{Na}}$  formulation by Ebihara and Johnson (11), which is fitted to data from embryonic chicken heart cells to which a slow inactivation gate  $j$ , as first proposed by Beeler and Reuter (1), was added. A detailed listing of all equations can be found in the APPENDIX.

## Membrane Currents

**Fast  $\text{Na}^{+}$  current:  $I_{\text{Na}}$ .** We use the three gates formulation of  $I_{\text{Na}}$  first introduced by Beeler and Reuter (1)

$$I_{\text{Na}} = G_{\text{Na}} m^3 h j (V - E_{\text{Na}}) \quad (4)$$

where  $m$  is an activation gate,  $h$  is a fast inactivation gate, and  $j$  is a slow inactivation gate. Each of these gates is governed by Hodgkin-Huxley-type equations for gating variables and characterized by a steady-state value and a time constant for reaching this steady-state value, both of which are functions of membrane potential (see APPENDIX).

The steady-state activation curve ( $m_{\infty}^3$ ) is fitted to data on steady-state activation of wild-type human  $\text{Na}^{2+}$  channels expressed in HEK-293 cells from Nagatomo et al. (44). Experimental data were extrapolated to  $37^{\circ}$ . Because there is no equivalent to the  $Q_{10}$  values used to extrapolate time constants to different temperatures, a linear extrapolation was used based on a comparison of values obtained at  $23^{\circ}$  and  $33^{\circ}$ . Note that similar  $\text{Na}^{+}$  channel activation data were obtained by others (64, 40, 55). Figure 1A shows the steady-state activation curve used in our model. For comparison, temperature-corrected experimental data are added.

The steady-state curve for inactivation ( $h_{\infty} \times j_{\infty}$ ) is fitted to steady-state inactivation data from Nagatomo et al. (44). Again, data were extrapolated to  $37^{\circ}$ . Similar inactivation data were obtained by others (55, 64). Figure 1B shows the steady-state inactivation curve used in our model together with temperature-corrected experimental data. Note that for resting membrane potentials the  $h$  and  $j$  gates are partially inactivated.

The time constants  $\tau_h$  and  $\tau_j$  are derived from current decay (typically  $V$  greater than  $-50$  mV) and current recovery experiments (typically  $V$  less than  $-80$  mV) (40, 44, 55, 58, 63–65). In both types of experiments a double-exponential fit is made to the data, allowing interpretation of the fast and slow inactivation time constants as  $\tau_h$  and  $\tau_j$ , respectively. To convert all data to  $37^{\circ}$  a  $Q_{10} = 2.79$  (derived from a comparison of fast inactivation time constants obtained at  $23^{\circ}$  and  $33^{\circ}$  by Nagatomo et al.) was used. Figure 1D shows our fit for the fast inactivation time constants, and Fig. 1E shows our fit for the slow inactivation time constants of the model. Temperature-adjusted experimental data points are added for comparison.

Activation time constants are derived from time to peak data from Nagatomo et al., converted as discussed above to  $37^{\circ}$ .  $\tau_m$  can be calculated from the peak time (where  $dI_{\text{Na}}/dt = 0$ ), assuming that  $j$  is constant and knowing  $m_{\infty}$ ,  $h_{\infty}$  and  $\tau_h$ . Figure 1C shows our fit of  $\tau_m$  together with experimentally derived, temperature-corrected time constants.

In Fig. 1F the time course of recovery from inactivation for our  $I_{\text{Na}}$  is shown. Recovery from inactivation was established by applying a double-pulse protocol: from the holding potential, a 1-s duration pulse to  $-20$  mV was applied to fully inactivate  $I_{\text{Na}}$ , the voltage was then stepped back to the holding potential to allow  $I_{\text{Na}}$  to recover for variable durations, and finally a second 30-ms pulse to  $-20$  mV was applied. The  $I_{\text{Na}}$  elicited during the second pulse is normalized relative to the  $I_{\text{Na}}$  elicited during the first pulse to establish the amount of recovery. Figure 1F shows normalized  $I_{\text{Na}}$  as a function of the duration of the recovery interval between the two pulses for various values of the holding potential. Similar to experimental observations by Viswanathan et al. (63), Nagatomo et al. (44), Schneider et al. (58), and Makita et al. (40), recovery is slower for higher recovery potentials and has a sigmoid shape when plotted on a logarithmic scale. Note that in experiments  $I_{\text{Na}}$  recovery is often slower than observed in our model, because our model is at physiological temperature whereas most experiments are performed at room temperature.

Figure 1G displays the rate dependence of the  $I_{\text{Na}}$  current. Rate dependence was tested by applying 500-ms pulses to  $-10$  mV from a holding potential of  $-100$  mV with different interpulse intervals. Steady-state current was normalized to the current elicited by the first pulse. The graph shows that for increasing frequency (decreasing



interpulse interval)  $I_{Na}$  decreases and that this decrease is considerably faster for 21° than for 37°. Experiments performed by Wang et al. (65) at 32° with an interpulse interval of 20 ms (1.92 Hz) show a reduction to 0.17 of the original current level, which lies between the reduction to 0.5 we measure at 37° and the reduction to 0.13 we measure at 21°.

For comparison purposes we also added LR  $m_\infty$ ,  $h_\infty$ ,  $\tau_m$ ,  $\tau_h$ , and  $\tau_j$  curves to Fig. 1, A–E. The following observations can be made. Our steady-state activation curve lies 8 mV to more negative potentials (Fig. 1A). Our steady-state inactivation curve lies 12 mV to more negative potentials (Fig. 1B). Activation time constants are in the same range of values (Fig. 1C). Our  $\tau_h$  curve has a similar shape, but for voltages smaller than –40 mV time constants are a factor of 1.6 larger, resulting in slower recovery dynamics (Fig. 1D). Similarly, our  $\tau_j$  is a factor of 3–5 larger for voltages smaller than –30 mV, leading to a considerably slower recovery from inactivation (Fig. 1E).  $G_{Na}$

was fitted to reproduce a  $\dot{V}_{max} = 260$  mV/ms, which is in the range of experimental data found by Drouin et al. (10).

**L-type  $Ca^{2+}$  current:  $I_{CaL}$ .** The L-type calcium current is described by the following equation

$$I_{CaL} = G_{CaL} d f_{Ca}^4 \frac{VF^2}{RT} \frac{Ca_i e^{2VF/RT} - 0.341 Ca_o}{e^{2VF/RT} - 1} \quad (5)$$

where  $d$  is a voltage-dependent activation gate,  $f$  is a voltage-dependent inactivation gate,  $f_{Ca}$  is an intracellular calcium-dependent inactivation gate, and driving force is modeled with a Goldman-Hodgkin-Katz equation.

The steady-state activation  $d_\infty$  and steady-state voltage inactivation curve  $f_\infty$  are fitted to  $I_{CaL}$  steady-state data from human ventricular myocytes reported by Benitah et al. (2), Mewes and Ravens (41), Pelzmann et al. (46), and Magyar et al. (39). Figure 2A shows the steady-state activation, and Fig. 2B shows the steady-state inactivation curve of our model together with experimental data from Pelzmann et al. (46).

Experimental data show that calcium-mediated inactivation is rapid, increases with calcium concentration, but is never complete (20, 60). More quantitative data about the precise dependence of amount and speed of inactivation on calcium concentration are unavailable and hard to obtain because intracellular calcium cannot be clamped to a constant value. As shown in Fig. 2C our  $f_{Ca}$  curve has a switchlike shape, switching from no inactivation to considerable but incomplete inactivation if calcium concentration exceeds a certain threshold. For suprathreshold concentrations the amount of inactivation depends mildly on calcium concentration.

There are hardly any experimental data on activation times of  $I_{CaL}$  in human myocytes. Therefore, as was done in the CRN model, we used the curve from the phase-2 LR model. Limited data on  $I_{CaL}$  activation times from Pelzmann et al. (46) were used to adjust the shape of the  $\tau_d$  curve of the LR model. Figure 2D displays the voltage-dependent activation time constant of our model.

The time constant  $\tau_{fca}$  is derived from experiments performed by Sun et al. (60). They show that during current decay experiments a fast and a slow time constant can be distinguished, with the fast time constant being independent of voltage and depending only on calcium, allowing interpretation as  $\tau_{fca}$ . Sun et al. (60) find a time constant of ~12 ms at 23°; no data on the concentration dependence of the time

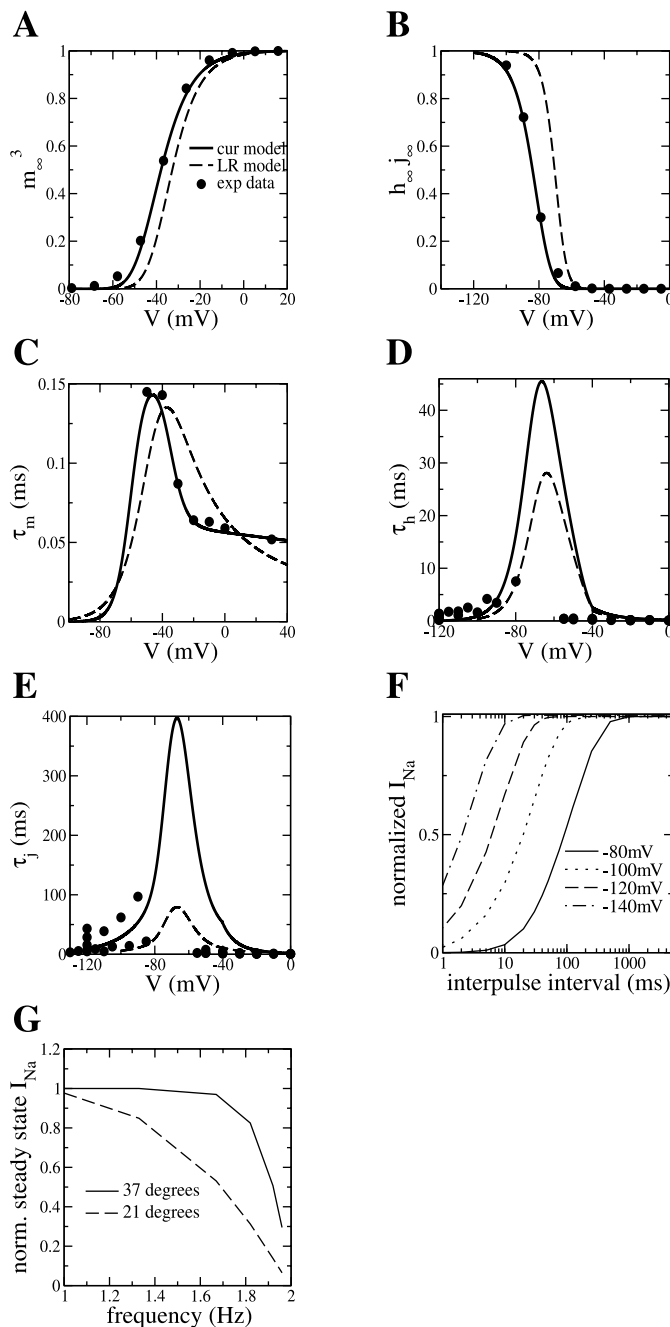


Fig. 1. Steady-state and time constant curves describing the gating of the fast sodium current. Model curves of our model (cur model) and the Luo-Rudy (LR) model are shown together with experimental data. A: steady-state activation curves. Experimental data are from Nagatomo et al. (44) and are extrapolated to 37°. B: steady-state inactivation curves. Experimental data are from Nagatomo et al. C: activation time constants. Experimental activation time constants are derived from time to peak data from Nagatomo et al. Experimental data are converted to 37° ( $Q_{10} = 2.79$ ). D: fast inactivation time constants. E: slow inactivation constants. Fast and slow experimental inactivation time constants are taken from Nagatomo et al. (44), Schneider et al. (58), Sakakibara et al. (55), Makita et al. (40), Wan et al. (64), Viswanathan et al. (63), and Wang et al. (65). Experimental time constants are converted to 37° ( $Q_{10} = 2.79$ ). F: recovery from inactivation for different recovery potentials. The time course of recovery from inactivation was established using a double-pulse protocol: from the holding potential a first 1-s duration pulse to –20 mV was applied to fully inactivate  $I_{Na}$ , then voltage was stepped back to the holding potential to allow recovery for periods ranging from 1 ms to 5 s, and finally a second 30-ms pulse to –20 mV was applied to measure the amount of recovery.  $I_{Na}$  elicited by the second pulse was normalized to the  $I_{Na}$  elicited by the first pulse and is shown as a function of recovery time. G: frequency dependence of  $I_{Na}$ . From a holding potential of –100 mV, 500-ms pulses to –10 mV are given with interpulse intervals of 10, 20, 50, 100, 250, and 500 ms, corresponding to stimulus frequencies of 1.96, 1.92, 1.82, 1.67, 1.3, and 1 Hz. The steady-state  $I_{Na}$  obtained for the different frequencies is normalized to the  $I_{Na}$  elicited by the first pulse. Frequency dependence was determined for 37° and 21°. For the 21° experiments gate dynamics were adapted with a  $Q_{10} = 2.79$ .

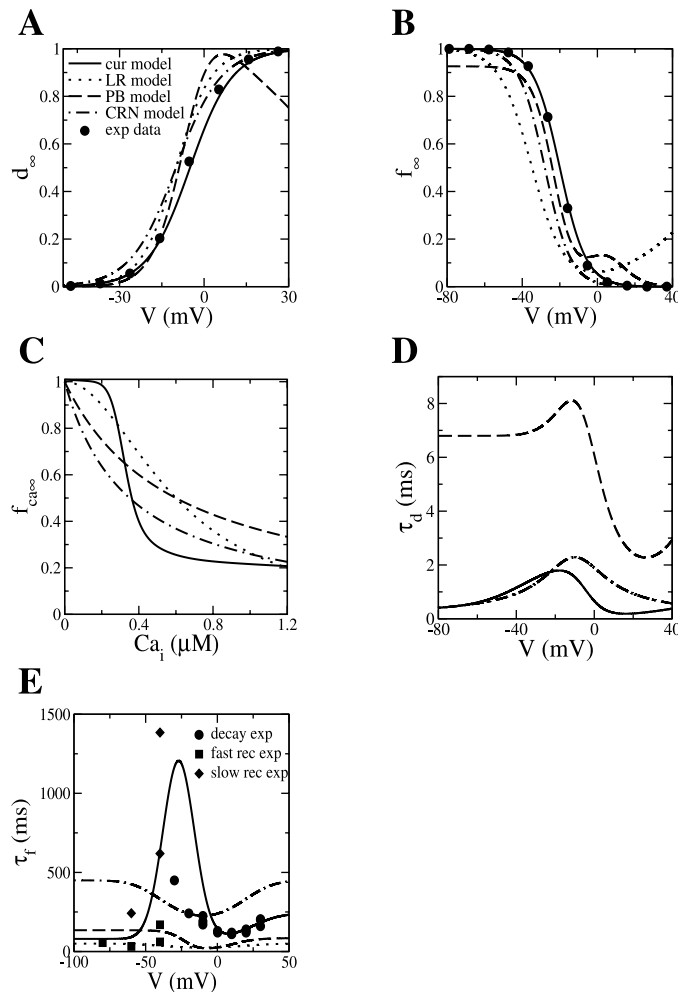


Fig. 2. Steady-state and time constant curves describing the gating of the L-type calcium current. Model curves of our model (cur model), the LR model, the PB model, and the CRN model are shown together with experimental data. A: steady-state voltage activation curves. Experimental steady-state activation data are from Pelzmann et al. (46). B: steady-state voltage inactivation curves. Experimental steady-state inactivation data are from Pelzmann et al. C: steady-state calcium inactivation curves. D: voltage activation time constants. Note that the LR and CRN models have the same time constant formulation: curves are overlapping. E: voltage inactivation time constants. Experimental inactivation time constants are taken from Beuckelmann et al. (4), Benitah et al. (2), Mewes et al. (41), Sun et al. (60), Li et al. (35), Pelzmann et al. (46), and Magyar et al. (39). Experimental data are converted to 37° degrees ( $Q_{10} = 2.1$ ). In addition, time constants derived from current decay experiments ( $V$  less than  $-30$  mV) are also corrected for the presence of extracellular calcium (correction factor 2.2). For an explanation of the latter, see text.

constant is available. We assumed a single time constant of 2 ms to be reasonable at 37°, comparable to the immediate inactivation used in the PB model and the 2-ms time constant used in the CRN model.

The time constants  $\tau_f$  are derived from experiments on calcium current decay and recovery in human ventricular and atrial myocytes by Beuckelmann et al. (4), Benitah et al. (2), Mewes et al. (41), Sun et al. (60), Li and Nattel (35), Pelzmann et al. (46), and Magyar et al. (39). Sun et al. (60) show that during current decay experiments the slow inactivation time constant depends both on voltage and extracellular calcium. After removal of extracellular calcium, an even slower, purely voltage-dependent inactivation time constant arises. It is this time constant that should be interpreted as  $\tau_f$ . Therefore, slow inactivation time constants found in current decay experiments were not only converted to 37° with a  $Q_{10} = 2.1$  (based on a comparison of time constants obtained by Li et al. and

Pelzmann et al. at physiological temperatures and data obtained by Benitah et al. at 21°) but were also corrected for the presence of extracellular  $Ca^{2+}$  with a slowing-down correction factor of 2.2 (based on a comparison of time constants obtained under normal conditions and under conditions in which extracellular  $Ca^{2+}$  was replaced by  $Sr^{2+}$  performed by Sun et al.).

In current recovery experiments also, two time constants are derived. However, assuming that recovery from calcium inactivation is fast and given the clear voltage dependence of both fast and slow recovery time constants, both can be considered as voltage-dependent time constants. Because our formulation of  $I_{CaL}$  incorporates only a single voltage-dependent inactivation gate, our  $\tau_f$  is constructed to form an intermediate between these fast and slow recovery time constants ( $-40 < V < -80$  mV). Figure 2E displays the voltage-dependent inactivation time constant of our model. For comparison, experimentally found inactivation time constants are added.

For comparison purposes we also added LR phase-2, PB, and CRN model curves for  $d_{\infty}$ ,  $f_{\infty}$ ,  $f_{Ca\infty}$ ,  $\tau_d$ , and  $\tau_f$  to Fig. 2, A–E. From this the following observations can be made. Our steady-state activation curve is similar to the curves used in the LR and CRN model. The PB model has, for unknown reasons, a curve with a somewhat different shape (Fig. 2A). Our steady-state inactivation curve inactivates completely, similar to the curve used in the CRN model, whereas the LR and PB model use incompletely inactivating curves (Fig. 2B). In experiments, inactivation is more complete if prepulse duration is longer or temperature is higher (35, 60), implying that inactivation is slow rather than incomplete.

Our  $f_{Ca\infty}$  curve has a switch shape, with a high level of inactivation beyond the threshold, whereas the LR, PB, and CRN curves are gradually declining functions of calcium (Fig. 2C). The high level of calcium inactivation, together with slow voltage inactivation, causes calcium to be the dominant mechanism of  $I_{CaL}$  inactivation in our model. This agrees well with experimental data. Incorporating calcium-dominated inactivation in models without local control may easily result in AP instability: in a local control model (21, 53)—in which individual  $I_{CaL}$  and calcium-induced calcium release (CICR) channels interact in subspaces—a smaller  $I_{CaL}$  current implies fewer open channels and hence fewer local calcium transients (sparks); the individual sparks still have the same effectiveness in closing nearby calcium channels. However, in a nonlocal control model, a smaller  $I_{CaL}$  generates a smaller global calcium transient that might be less effective in inactivating the  $I_{CaL}$  current. By using a switch shape for  $f_{Ca\infty}$ , we ensure effective calcium inactivation for a wide range of systolic calcium levels in our model.

The  $\tau_d$  curve of our model has a similar shape as that used in the PB model, but with a factor of 2–3 shorter time constants, and is a minor adaptation of the curves used in the LR and CRN model (Fig. 2D). Our  $\tau_f$  curve, which is fitted to the experimental data, has a maximum between  $-50$  and  $0$  mV, whereas the curves used in the LR, PB, and CRN models have a minimum in this voltage region, in strong contrast with the experimental data (Fig. 2E). The  $f$  gate inactivation in our model is much slower than in the LR and PB model;  $f$  gate inactivation in the CRN model is even slower. The slow  $f$  gate inactivation in our model and the CRN model is important for making calcium the dominant mechanism of  $I_{CaL}$  inactivation. The  $f$  gate recovery in our model is similar to that in the LR and PB model and a factor of 4 faster than in the CRN model. It plays an important role in determining APDR, which in our model agrees well with experimental data (see Fig. 8).  $P_{CaL}$  is fitted to reproduce peak current values found by Li et al. (35) under physiological temperatures.

We modeled the driving force of the calcium current with the Goldman-Hodgkin-Katz equation. For simplicity, we ignored the small permeability the channel also has for sodium and potassium ions. In the Luo-Rudy phase-2 model, a Goldman-Hodgkin-Katz-like equation for calcium, sodium, and potassium is used. In the PB and CRN models, a constant-valued reversal potential is used.

**Transient outward current:  $I_{to}$ .** For  $I_{to}$  the following formulation is used

$$I_{to} = G_{to}rs(V - E_K) \quad (6)$$

where  $r$  is a voltage-dependent activation gate and  $s$  is a voltage-dependent inactivation gate.

The steady-state activation curve ( $r_\infty$ ) is fitted to data on steady-state activation of  $I_{to}$  current in human ventricular myocytes of epicardial and endocardial origin at 35° from Nabauer et al. (43). Because no significant difference between activation in epicardial and endocardial cells was found, a single formulation was used. Figure 3A shows the steady-state activation curve used in the model together with experimental data. A 10-mV positive shift was performed on the experimental data to account for the use of  $Cd^{2+}$  to block  $I_{CaL}$  current, similar to the approach taken by Courtemanche et al. (8). The greater steepness of the model curve relative to the experimental curve was necessary to make sure that no significant reactivation of  $I_{to}$  occurs on repolarization.

The steady-state inactivation curve ( $s_\infty$ ) is fitted to data on steady-state inactivation from Nabauer et al. Because of significant differ-

ences between curves obtained for epicardial and endocardial cells, two separate model formulations were used. Figure 3B shows the steady-state inactivation curves used in the model together with  $Cd^{2+}$ -corrected experimental data.

Inactivation time constants are fitted to data from Nabauer et al. (43) and Wettwer et al. (68). Current decay experiments show similar time constants for epicardial and endocardial  $I_{to}$ , whereas current recovery experiments show much slower recovery from inactivation for endocardial than epicardial  $I_{to}$ , thus making two separate formulations for  $\tau_s$  necessary. Figure 3D shows our fits for epicardial  $\tau_s$ , and Fig. 3E shows our fit for endocardial  $\tau_s$ . For comparison, experimental inactivation time constants are added.

Activation time constants are derived from time to peak data from expression of hKv4.3-2—encoding an epicardial type transient outward channel—in mouse fibroblast cells by Greenstein et al. (22) in a manner similar to the derivation of  $\tau_m$ . Figure 3C shows our  $\tau_r$  curve together with experimentally derived time constants.

For comparison purposes we also added PB and CRN model curves for  $r_\infty$ ,  $s_\infty$ ,  $\tau_r$ , and  $\tau_s$  to Fig. 3, A–D. From this the following observations can be made. The steady-state activation of our model almost coincides with that of the PB model and has a steeper slope and more positive half-activation point than that of the CRN model (Fig. 3A). In our model we distinguish epicardial and endocardial steady-state inactivation, whereas the PB and CRN model only have a single steady-state inactivation curve. The epicardial steady-state inactivation of our model lies 15 and 25 mV to more positive potentials than the curves used in the PB and CRN models, respectively. For the endocardial steady-state inactivation of our model these numbers are 8 and 18 mV, respectively (Fig. 3B).

The activation time constant of our model results in faster inactivation and slower recovery than that of the PB model, whereas it is a factor of 2 slower than the CRN model time constant (Fig. 3C). However, in the CRN model three activation gates are used ( $r^3$ ), causing net activation to be slower and net deactivation to be faster than that of a single gate and thus complicating the comparison. In our model we distinguish epicardial and endocardial inactivation time constants, whereas the PB and CRN model only have a single inactivation time constant. The inactivation time constant of the PB model resembles our epicardial inactivation time constant in magnitude but has hardly any voltage dependence. The inactivation time constant of the CRN model is similar to our epicardial inactivation time constant (Fig. 3D).

$G_{to}$  is fitted to experimental data on current density from Wettwer et al. (68) and Nabauer et al. (43). Both show large differences in  $I_{to}$  size between epicardial and endocardial cells. We use  $G_{to} = 0.294$  nS/pF for epicardial and  $G_{to} = 0.073$  nS/pF for endocardial cells (25% of the value for epicardial cells). Figure 4 shows the current voltage ( $I$ - $V$ ) relationships for epicardial (Fig. 4A) and endocardial (Fig. 4B)  $I_{to}$  together with experimental data from Nabauer et al. (43).

We assume that  $I_{to}$  is specific for potassium ions and used the reversal potential  $E_K$ . A similar approach is taken in the CRN model, whereas in the PB model it is assumed that the channel is also permeable to sodium ions.

**Slow delayed rectifier current:**  $I_{Ks}$ . For the slow delayed rectifier current the following formulation is used

$$I_{Ks} = G_{Ks}x_s^2(V - E_{Ks}) \quad (7)$$

where  $x_s$  is an activation gate and  $E_{Ks}$  is a reversal potential determined by a large permeability to potassium and a small permeability to sodium ions (see APPENDIX).

The steady-state activation curve ( $x_{s\infty}$ ) is fitted to  $I_{Ks}$  activation data obtained for human ventricular myocytes at 36° from Li et al. (34). In Fig. 5A the steady-state activation curve used in the model is shown together with the experimental data.

Activation time constants are based on data from Virag et al. (62) and Wang et al. (66). Both sets of data were obtained in human ventricular myocytes at physiological temperatures. Figure 5B shows

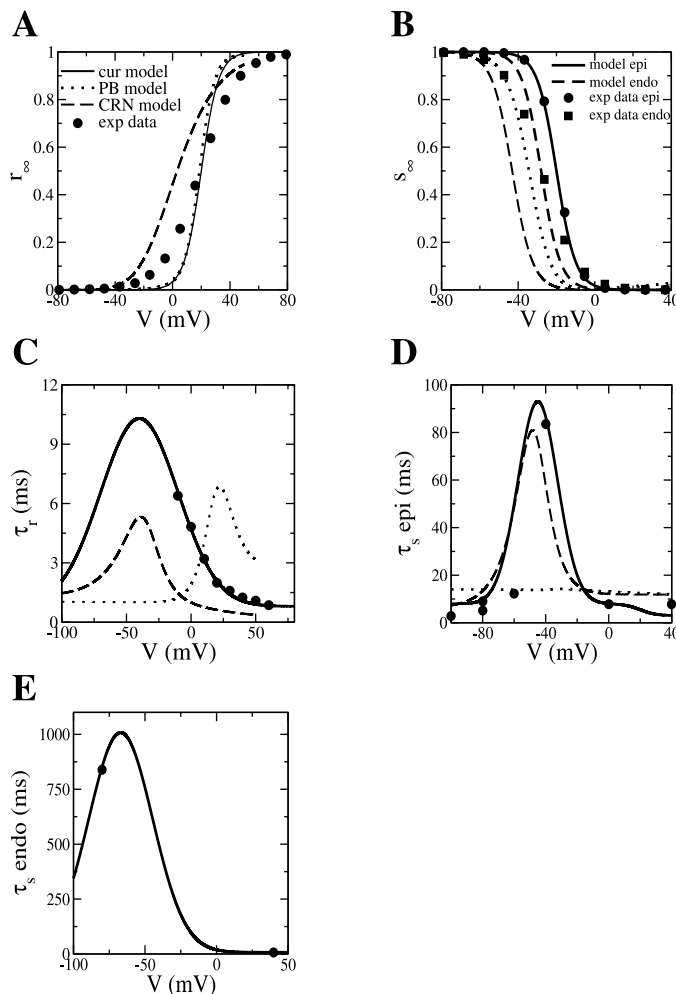


Fig. 3. Steady-state and time constant curves describing the gating of the transient outward current. Model curves of our model (cur model), the PB, and the CRN model are shown together with experimental data. A: steady-state activation curves. Experimental steady-state data are from Nabauer et al. (43). A 10-mV positive shift was performed on the experimental curve to account for the use of  $Cd^{2+}$ . B: steady-state inactivation curves.  $Cd^{2+}$ -corrected experimental data are from Nabauer et al. C: activation time constants. Experimental activation time constants are derived from time to peak data by Greenstein et al. (22). D: epicardial inactivation time constants. Experimental inactivation time constants are from Nabauer et al. and are obtained at physiological temperatures. E: endocardial inactivation time constant. Experimental data are from Nabauer et al.

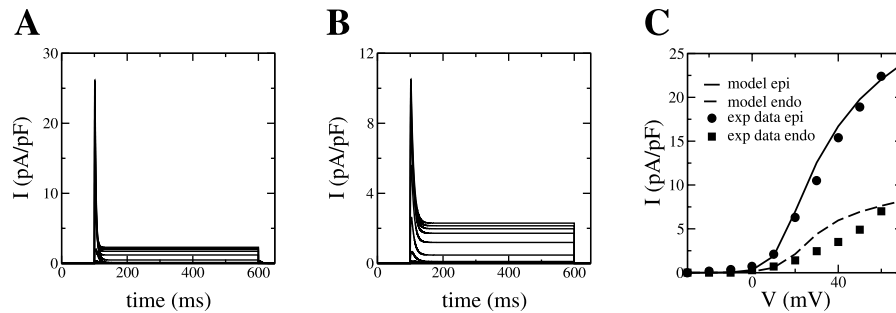


Fig. 4. *A* and *B*: epicardial (*A*) and endocardial (*B*)  $I_{to}$  current traces generated by the model during simulated voltage-clamp experiments. Currents are recorded during 500-ms voltage steps to potentials ranging from  $-30$  to  $80$  mV from a holding potential of  $-80$  mV and an intermittent 100-ms prepulse to  $-60$  mV. Note that during simulation both the  $I_{to}$  and  $I_{pK}$  currents were switched on. The sustained part of the current traces is generated by  $I_{pK}$ . *C*: epicardial and endocardial  $I_{to}$  current-voltage ( $I-V$ ) curves obtained from the series of experiments shown in *A* and *B*, respectively. Peak current minus maintained current was measured. Experimental  $I-V$  curves from Nabauer et al. (43), obtained with a similar voltage-clamp protocol, are added for comparison. The experimental curves are rescaled by a factor of 1.4. We choose  $I_{to}$  density to be somewhat larger than experimentally found to obtain a realistic notch in epicardial action potential morphology.

our fit of  $\tau_{xs}$ . Experimentally obtained activation time constants are added for comparison.

Fitting  $G_{Ks}$  to experimentally obtained current densities would result in a small  $I_{Ks}$  that has little effect on APD: simulating M cells by a 75% reduction in  $I_{Ks}$  density (the principal difference with epicardial cells) would result in M cell APD being only 10 ms longer than epicardial APD, in strong contrast with the 100-ms difference in APD found experimentally (9, 36). Thus there is a discrepancy between current density measured in voltage-clamp experiments and the apparent contribution of the current to APD. This discrepancy is probably due to sensitivity of  $I_{Ks}$  channels to the cell isolation procedures used for voltage-clamp experiments (70), resulting in considerable degradation of  $I_{Ks}$  channels before current density measurements. Therefore, instead of fitting  $G_{Ks}$  to voltage-clamp data, we based it on APD measurements: by using a  $G_{Ks} = 0.327$  nS/pF for epicardial cells and a  $G_{Ks} = 0.082$  nS/pF in M cells, we get an epicardial APD at 1 Hz of 276 ms and an M cell APD of 336 ms, resulting in an APD difference of 60 ms, which is in the range of experimental values (9, 36). This approach of basing a conductance value on electrophysiological properties rather than measured current density is also used in the development of other models; e.g., in the CRN model,  $G_{Na}$  is fitted to get the right  $\dot{V}_{max}$ ,  $G_{to}$  to get the right AP morphology, and  $G_{Kr}$  and  $G_{Ks}$  to get the right APD (8) and in a later version of the LR model in which  $I_K$  was replaced by  $I_{Kr}$  and  $I_{Ks}$ ,  $G_{Ks}$  was fitted to get the right APD prolongation if  $I_{Ks}$  current is blocked

(71). In addition, the values used for  $G_{Ks}$  and  $G_{Kr}$  in the CRN model and the LR model are similar to the values we use in our model. In Fig. 5C the  $I-V$  relationship of  $I_{Ks}$  is shown together with rescaled experimental data from Li et al.

We use a sodium-to-potassium permeability ratio of  $p_{KNa} = 0.03$ , resulting in a reversal potential  $E_{Ks}$  that forms a compromise between reversal potentials found experimentally (34, 62). In the PB model a permeability ratio of 0.018 is used, whereas in the CRN model it is assumed that  $I_{Ks}$  is permeable to potassium ions only. Our steady-state activation curve lies 5 and 15 mV to more positive potentials than the curves used in the CRN and PB models, respectively. Compared with the  $\tau_{xs}$  formulations used by both of these models, our  $I_{Ks}$  displays slower activation and more rapid deactivation.

**Rapid delayed rectifier current:  $I_{Kr}$ .** The rapid delayed rectifier current is described by the following equation

$$I_{Kr} = G_{Kr} \sqrt{\frac{K_o}{5.4}} x_{r1} x_{r2} (V - E_K) \quad (8)$$

where  $x_{r1}$  is an activation gate and  $x_{r2}$  is an inactivation gate.  $\sqrt{K_o/5.4}$  represents the  $K_o$  dependence of the current. Note that because no data are available on the  $K_o$  dependence of human ventricular  $I_{Kr}$ , a similar dependence as measured in and implemented for animal myocytes is assumed (38).

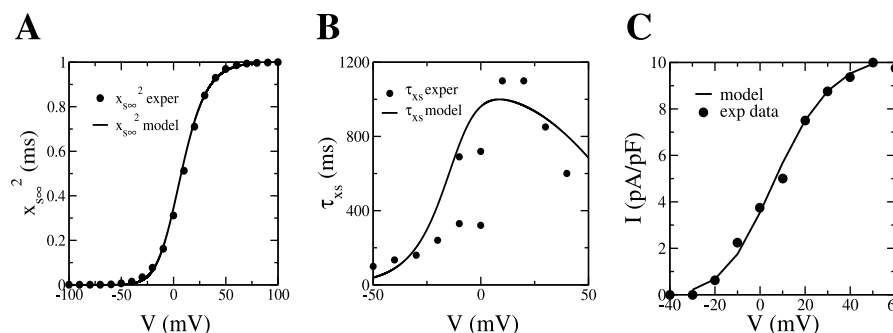


Fig. 5. Steady-state and time constant curves describing the gating of the slow delayed rectifier current. *A*: steady-state activation curve. Experimental steady-state data are from Li et al. (34). *B*: activation time constants. Experimental activation time constants are from Virag et al. (62) (for voltages ranging from  $-50$  to  $0$  mV) and Wang et al. (66) (for voltages ranging from  $-10$  to  $40$  mV) and are obtained at physiological temperatures. *C*:  $I-V$  relationship for  $I_{Ks}$ . Tail currents are measured during 5,000-ms voltage steps to potentials ranging from  $-10$  to  $50$  mV from a holding potential of  $-40$  mV. Experimental  $I-V$  curves obtained with a similar protocol by Li et al. (34) were included for comparison. Experimental data are rescaled by a factor of 12.5. See text for an explanation of why our model  $I_{Ks}$  is much larger than the experimentally measured  $I_{Ks}$ .



The steady-state activation curve ( $x_{r1}^\infty$ ) is fitted to activation data on the expression of HERG channels in HEK 293 cells by Zhou et al. (72), in Chinese hamster ovary cells by Johnson et al. (28), and in *Xenopus* oocytes by Smith and Yellen (59). Steady-state inactivation ( $x_{r2}^\infty$ ) is fitted to data from Johnson et al. (28) and Smith and Yellen (59). Figure 6A shows steady-state curves of the model together with experimental data.

Activation time constants ( $\tau_{xr1}$ ) are fitted to data from Zhou et al. (72) obtained at physiological temperatures.  $\tau_{xr12}$  is fitted to inactivation time constants obtained at physiological temperatures by Johnson et al. (28). Figure 6B shows our fit of  $\tau_{xr1}$ , and Fig. 6C shows our fit of  $\tau_{xr2}$ . Experimentally obtained time constants are added for comparison.

Fitting  $G_{Kr}$  to experimentally obtained current densities would result in an  $I_{Kr}$  that has a lower contribution to APD than suggested by experiments in which  $I_{Kr}$  is blocked (34). Therefore, similar to our approach for  $G_{Ks}$ , we used such a value for  $G_{Kr}$  (0.128 nS/pF) that a complete blocking of  $I_{Kr}$  leads to 44 ms of APD prolongation, which is in the range of values found experimentally by Li et al. (34). The  $I$ - $V$  relationship of  $I_{Kr}$  is shown in Fig. 6D. For comparison, rescaled experimental data from Iost et al. (25) and Li et al. (34) are added. Note that our model curve is shifted toward more negative potentials relative to the experimental curves. This difference may be due to the fact that we fitted  $I_{Kr}$  to data from expression experiments in hamster and *Xenopus* cells, whereas the experimental  $I$ - $V$  curves are from experiments on human cardiac cells.

The steady-state activation curve of our  $I_{Kr}$  lies 10 and 20 mV to more negative potentials than the curves used in the PB and CRN

models, respectively.  $\tau_{xr1}$  has a size and a shape similar to those used in these two models. We modeled inward rectification as a time-dependent inactivation gate, whereas the PB and the CRN model implemented this inactivation as being instantaneous. Our steady-state inactivation curve lies 50 and 60 mV to more negative potentials than the inward rectification curves used in the PB and CRN models, which seem to have no clear experimental basis.

**Inward rectifier  $K^+$  current:**  $I_{K1}$ . For  $I_{K1}$  the following formulation is used

$$I_{K1} = G_{K1} \sqrt{\frac{K_o}{5.4}} x_{K1\infty} (V - E_K) \quad (9)$$

where  $x_{K1\infty}$  is a time-independent inward rectification factor that is a function of voltage.  $\sqrt{K_o/5.4}$  represents the  $K_o$  dependence of the current. As for  $I_{Kr}$ , because of a lack of data on  $K_o$  dependence of human  $I_{K1}$  we assumed a dependence similar to that in animal myocytes.

Experimental data on  $I_{K1}$  current size are highly variable, as previously discussed by Courtemanche et al. (8). We used the formulation for  $I_{K1}$  used in the PB model but increased  $G_{K1}$  by a factor of 2 to account for the larger current densities found by Koumi et al. (33) in the  $I_{K1}$ -relevant voltage range (−90 mV to −40 mV). This results in a value for  $G_{K1}$  that is approximately five times larger than in the CRN model, which agrees with data from Koumi et al. (33) showing that  $I_{K1}$  is a factor of 5.6 higher in human ventricular than in atrial myocytes.

**$Na^+/Ca^{2+}$  exchanger current,  $Na^+/K^+$  pump current, and plateau and background currents.** For  $I_{NaCa}$  the following equation is used

$$I_{NaCa} = k_{NaCa} \frac{e^{\gamma VF/RT} Na_i^3 Ca_o - e^{(\gamma-1)VF/RT} Na_o^3 Ca_i \alpha}{(K_{mNa}^3 + Na_o^3)(K_{mCa} + Ca_o)(1 + k_{sat} e^{(\gamma-1)VF/RT})} \quad (10)$$

This formulation is similar to the equation used in the LR model, except for the extra factor  $\alpha$  ( $= 2.5$ ) that accounts for the higher concentration of calcium in the subspace close to the sarcolemmal membrane where the  $Na^+/Ca^{2+}$  exchanger is actually operating. Our approach is similar to that used in the Noble et al. model with diadic subspace (45), where  $I_{NaCa}$  was made dependent on diadic calcium rather than bulk cytoplasmic calcium. Otherwise, during the AP plateau phase the increase in bulk cytoplasmic calcium is not enough to counteract the increase in voltage and  $I_{NaCa}$  current becomes outward oriented during a long period of the plateau phase, which is unrealistic (27).

For  $I_{NaK}$  we use the following formulation

$$I_{NaK} = R_{NaK} \frac{K_o Na_i}{(K_o + K_{mK})(Na_i + K_{mNa})(1 + 0.1245 e^{-0.1VF/RT} + 0.0353 e^{-VF/RT})} \quad (11)$$

This formulation is similar to the formulations used in the LR, PB, and CRN models.

For  $I_{pCa}$  the following commonly applied equation is used

$$I_{pCa} = G_{pCa} \frac{Ca_i}{K_{pCa} + Ca_i} \quad (12)$$

For  $I_{pK}$  the following equation is used

$$I_{pK} = G_{pK} \frac{V - E_K}{1 + e^{(25-V)/5.98}} \quad (13)$$

This is similar to the equation used by Luo and Rudy.

The background sodium and calcium leakage currents are given by the following equations

$$I_{bNa} = G_{bNa}(V - E_{Na}) \quad (14)$$

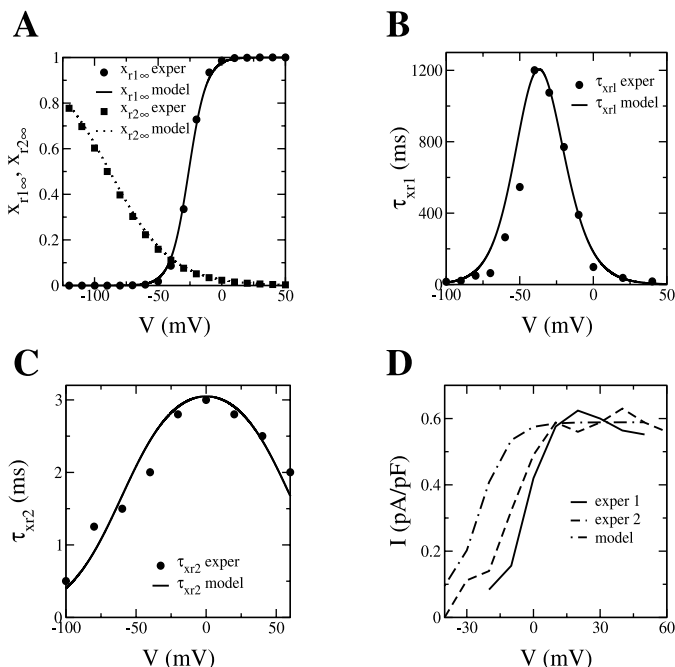


Fig. 6. Steady-state and time constant curves describing the gating of the rapid delayed rectifier current. A: steady-state activation and inactivation curves. Experimental data on steady-state activation are from Zhou et al. (72), experimental data on inactivation are from Johnson et al. (28) and Smith and Yellen (59). B: activation time constants. Experimental activation time constants are from Zhou et al. (72). C: inactivation time constants. Experimental inactivation time constants are from Johnson et al. (28). Experimental time constants are obtained at physiological temperatures. D:  $I$ - $V$  relationship for  $I_{Kr}$ . Tail currents are measured during 3,000-ms voltage steps to potentials ranging from −40 to 60 mV from a holding potential of −60 mV. For comparison experimental  $I$ - $V$  curves obtained using a similar protocol by Iost et al. (25) (exper 1) and Li et al. (34) (exper 2) are added. Experimental curves are rescaled by factors of 2.4 and 1.4, respectively. See text for an explanation of why our model  $I_{Kr}$  is larger than the experimentally measured  $I_{Kr}$ .



$$I_{bCa} = G_{bCa}(V - E_{Ca}) \quad (15)$$

For  $P_{NaCa}$ ,  $P_{NaK}$ ,  $G_{pCa}$ ,  $G_{pK}$ ,  $G_{bNa}$ , and  $G_{bCa}$ , values were chosen such that a frequency change results in  $Na_i$ ,  $K_i$ , and  $Ca_i$  transients with a time scale of  $\sim 10$  min, similar to experimental recordings (5) and which result in equilibrium concentrations—for different frequencies—that lie in the range of experimental observations (49). The values used lie in the range of values used in the PB and CRN models (for parameter values see Table 1).

**Intracellular ion dynamics.** The calcium dynamics of our model are described using the following set of equations

$$I_{leak} = V_{leak}(Ca_{sr} - Ca_i) \quad (16)$$

$$I_{up} = \frac{V_{maxup}}{1 + K_{up}^2/Ca_i^2} \quad (17)$$

$$I_{rel} = \left( a_{rel} \frac{Ca_{sr}^2}{b_{rel}^2 + Ca_{sr}^2} + c_{rel} \right) dg \quad (18)$$

$$Ca_{ibufc} = \frac{Ca_i \times Buf_c}{Ca_i + K_{bufc}} \quad (19)$$

$$\frac{dCa_{total}}{dt} = -\frac{I_{CaL} + I_{bCa} + I_{pCa} - 2I_{NaCa}}{2V_cF} + I_{leak} - I_{up} + I_{rel} \quad (20)$$

$$Ca_{srbufsr} = \frac{Ca_{sr} \times Buf_{sr}}{Ca_{sr} + K_{bufsr}} \quad (21)$$

$$\frac{dCa_{srtotal}}{dt} = \frac{V_c}{V_{SR}} (-I_{leak} + I_{up} - I_{rel}) \quad (22)$$

where  $I_{leak}$  is a leakage current from the sarcoplasmic reticulum to the cytoplasm,  $I_{up}$  is a pump current taking up calcium in the SR,  $I_{rel}$  is the calcium-induced calcium release (CICR) current,  $d$  is the activation gate of  $I_{CaL}$ , here reused as the activation gate of  $I_{rel}$ , following a similar approach as in Chudin et al. (7), and  $g$  is the calcium-dependent inactivation gate of  $I_{rel}$ .  $Ca_{total}$  is the total calcium in the cytoplasm, it consists of  $Ca_{ibufc}$ , the buffered calcium in the cytoplasm, and  $Ca_i$ , the free calcium in the cytoplasm. Similarly,  $Ca_{srtotal}$  is the total calcium in the SR, it consists of  $Ca_{srbufsr}$ , the buffered calcium in the SR, and  $Ca_{sr}$ , the free calcium in the SR. Ratios between free and buffered calcium are analytically computed assuming a steady-state for the buffering reaction (Eqs. 19 and 21), following the same approach as first used by Zeng et al. (71) (for a description and values of the parameters see Table 1). Our model for calcium dynamics has a complexity similar to that of most of the current models that are used to study the dynamics of wave propagation in cardiac tissue (LR, CRN, and PB models). Recently, complex models for intracellular calcium handling have been developed that model individual L-type calcium and ryanodine channels, discrete calcium release subunits, and sparks (53, 21). Because of their huge computational demands these models for calcium dynamics have not yet been incorporated in models for cardiac wave propagation.

The changes in the intracellular sodium ( $Na_i$ ) and potassium ( $K_i$ ) concentrations are governed by the following equations

$$\frac{dNa_i}{dt} = -\frac{I_{Na} + I_{bNa} + 3I_{NaK} + 3I_{NaCa}}{V_cF} \quad (23)$$

$$\frac{dK_i}{dt} = -\frac{I_{K1} + I_{to} + I_{Kr} + I_{Ks} - 2I_{NaK} + I_{pK} + I_{stim} - I_{ax}}{V_cF} \quad (24)$$

To avoid the model being overdetermined, as is the case for a lot of second-generation electrophysiological models (13, 14, 24), we followed the approach suggested by Hund et al. (24) and accounted for the external stimulus current ( $I_{stim}$ ) and the axial current flow ( $I_{ax}$ ) in the equation for  $K_i$  dynamics. As mentioned above, conductances of background leakage, plateau, and pump currents were chosen such

that transient time scales and equilibrium concentrations lie in the range of experimental observations.

## RESULTS

### Single Cell

Figure 7 shows an AP, a calcium transient, and the major ionic currents generated by the model under 1-Hz pacing for a parameter setting corresponding to a human epicardial ventricular cell. The AP shows the characteristic spike notch dome

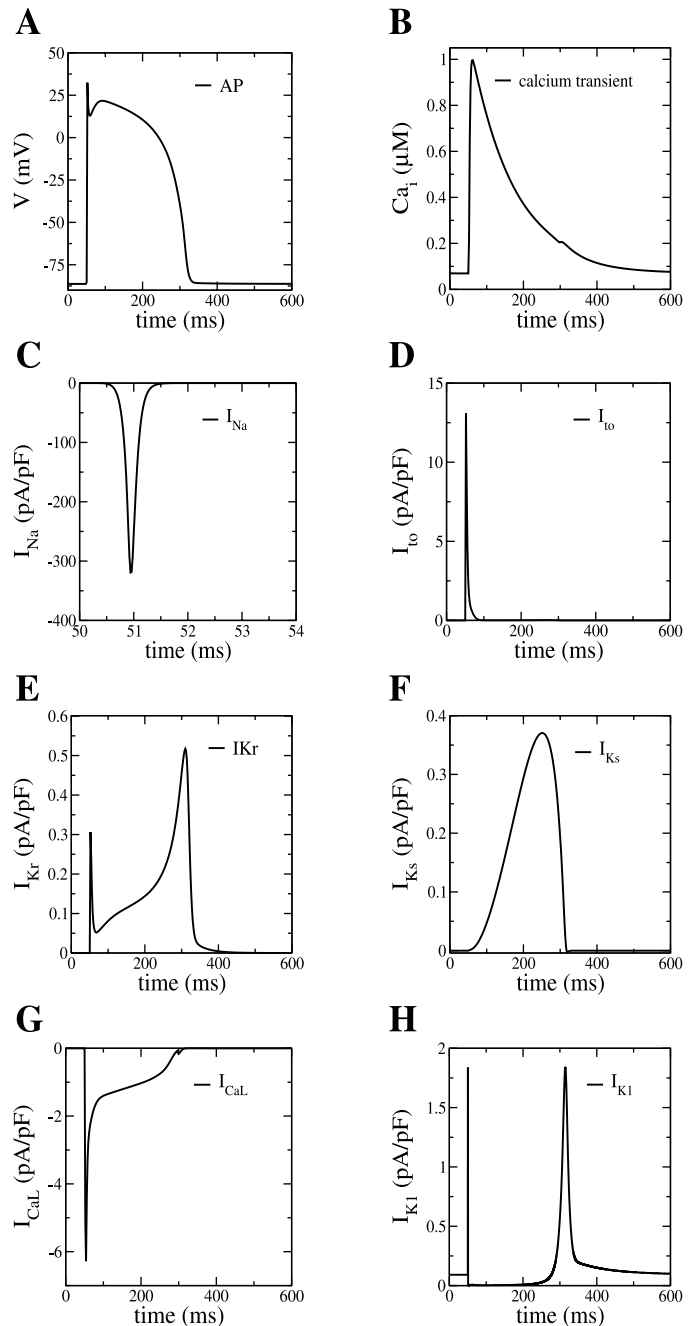


Fig. 7. Steady-state action potential, calcium transient, and major ionic currents under 1-Hz pacing. A: action potential. B: calcium transient. C: fast sodium current (note the difference in time scale used here). D: transient outward current. E: rapid delayed rectifier current. F: slow delayed rectifier current. G: L-type calcium current. H: inward rectifier current.

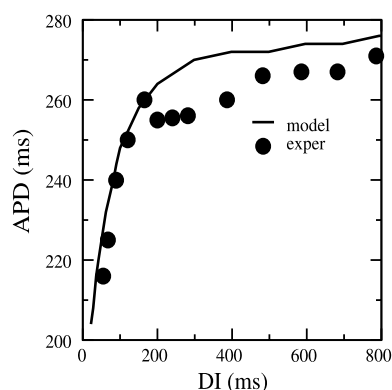


Fig. 8. Action potential duration (APD) restitution curve obtained by using the S1-S2 protocol with a basic cycle length of 1,000 ms. For comparison, experimental data from Morgan et al. (42) are included. DI, diastolic interval.

architecture found for epicardial cells. Resting potential is  $-87.3$  mV, maximum plateau potential is  $21.7$  mV, and  $\dot{V}_{\max} = 288$  mV/ms, all in agreement with experimental data (10, 36). The calcium transient shows the characteristic rounded-off triangular shape found in experiments. Diastolic calcium level is  $0.07$   $\mu\text{M}$  and maximum systolic calcium level under 1-Hz pacing is  $1.0$   $\mu\text{M}$ , comparable to values in the PB model and experimentally obtained values by Beuckelmann et al. (26). The ionic currents presented in Fig. 7 have shapes and values similar to those recorded experimentally. Note that the initial spikelike increase of  $I_{K_r}$  in our model is absent in the PB and CRN models. This initial increase is also observed in experiments (18, 72) and is achieved by modeling the inward rectification as a time-dependent process.

Figure 8 shows the APDR curve for a single epicardial cell obtained with the S1-S2 restitution protocol (see MATERIALS AND METHODS) with a basic cycle length (BCL) of 1,000 ms. For comparison, experimental data found by Morgan and coworkers (42) are added. It can be seen that the APDR curve of our model in a wide range closely matches the experimentally measured curve.

Figure 9A shows the change in diastolic and systolic calcium levels when pacing frequency is increased in a stepwise fashion from 0.25 to 0.5 to 1 to 1.5 to 2 to 2.5 to 3 Hz. From the figure it can be seen that systolic calcium level first increases substantially up to a frequency of 2 Hz, saturates, and then starts to decrease. In Fig. 9B the corresponding increase in intracellular sodium levels with increasing pacing frequency are shown. It can be seen that sodium keeps increasing but the speed of increase decreases for higher frequencies. Sodium

concentrations for different frequencies are in the range of values measured by Pieske et al. (49). Figure 9C shows the normalized systolic calcium level as a function of pacing frequency. Assuming that generated force is linearly dependent on systolic calcium, the calcium frequency staircase of our model is similar to the force-frequency relationship obtained experimentally for human myocardial cells by Pieske et al. (48, 49) and Schmidt et al. (57).

### Different Cell Types

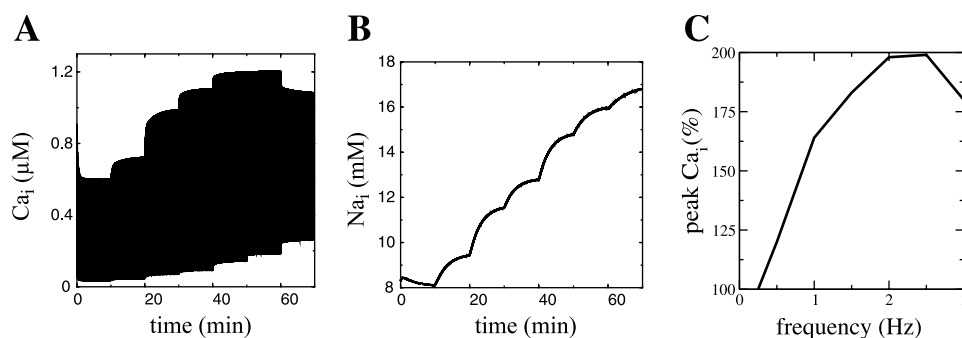
The parameter setting in *Single Cell* reproduces the AP of an epicardial cell. By changing a few parameters, our model is capable of reproducing the AP shapes of the two other ventricular cell types: endocardial and M cells.

In our model endocardial cells differ from epicardial cells in their lower  $I_{to}$  density ( $G_{to} = 0.073$  nS/pF instead of  $0.294$  nS/pF, factor 4 difference) and in their slower recovery from inactivation (different  $\tau_s$ , see APPENDIX). These differences are based on data from Nabauer et al. (43) and Wettwer et al. (68). According to Peyer et al. (47),  $I_{K_s}$  of epicardial and endocardial cells are similar. In our model, M cells differ from epicardial and endocardial cells by having an  $I_{K_s}$  density of  $0.062$  instead of  $0.245$  nS/pF (factor 4 difference). This is based on data from Peyer et al. (47). M cells have  $I_{to}$  density and dynamics similar to those of epicardial cells (36).

Figure 10 shows APs recorded under steady-state conditions at BCLs of 1,000, 2,000 and 5,000 ms for epicardial (Fig. 10A), endocardial (Fig. 10B), and M (Fig. 10C) cells. From a comparison of Fig. 10, A and B, it follows that the smaller  $I_{to}$  of endocardial cells results in the virtual absence of the notch that is clearly present in the APs of epicardial and M cells. From a comparison of Fig. 10, A and C, it follows that the smaller  $I_{K_s}$  of M cells results in a longer APD relative to epicardial and endocardial cells (336 ms in M cells vs. 276 ms in epicardial and 282 ms in endocardial cells for BCL = 1,000 ms) and in a stronger rate dependence of M cell APD.

Note that simulated APD and rate dependence differences between M cells and epi- and endocardial cells are a bit smaller than the experimentally observed differences (9, 36). This is probably due to the fact that M cells differ from the other cell types not only in their  $I_{K_s}$  density but also with respect to other current densities. Currently, differences in the late component of  $I_{Na}$  have been described for guinea pig (56) and canine myocardium (73), with guinea pig M cells having a smaller and canine M cells having a larger  $I_{Na,late}$  than the other cell types, and differences in the density of  $I_{NaCa}$  have been described for canine myocardium (74), with M cells having a larger ex-

Fig. 9. Changes in calcium dynamics under increasing pacing frequencies. Pacing frequency is varied from 0.25 to 3 Hz; each frequency is maintained for 10 min. A: positive contraction staircase: increase in calcium transient amplitude when pacing frequency is increased from 0.25 to 0.5 to 1 to 1.5 to 2 to 2.5 Hz. For the transition from 2.5 to 3 Hz, a mild decrease of systolic calcium level occurs. B: concurrent increase in intracellular sodium when pacing frequency is increased. C: normalized systolic calcium as a function of pacing frequency. Normalization relative to level at 0.25 Hz.



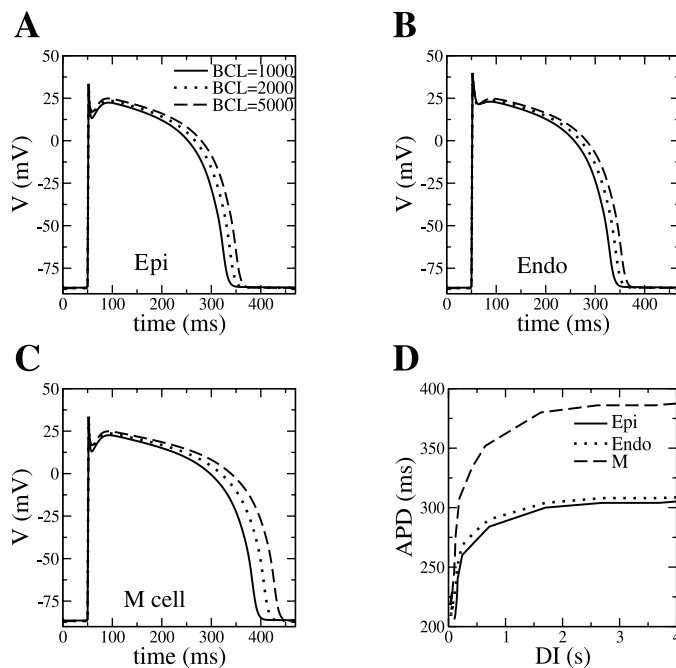


Fig. 10. Different behavior of epicardial, endocardial, and midmyocardial cell types. Steady-state action potentials for BCL of 1,000, 2,000, and 5,000 ms for epicardial (A), endocardial (B), and M (C) cells. D: APD restitution curves of the 3 cell types obtained with the dynamic restitution protocol.

changer current. Because of the partially contradictory nature of the data and the lack of data for human myocardium, we decided not to incorporate any of these other differences in our M cell description in the current version of our model.

Figure 10D shows restitution curves for epicardial, endocardial, and M cells obtained with the dynamic restitution protocol. Again, the longer APD and stronger rate dependence of M cells can be observed. In addition, we can see that the APD of endocardial cells is slightly longer than that of epicardial cells, because of the lower  $I_{to}$  density, and their APD rate dependence is slightly different, because of the slower  $I_{to}$  recovery dynamics. Results are very similar to experimentally obtained restitution curves by Drouin et al. (10).

### 1D Propagation

Figure 11 shows CV restitution curves for a cable of 400 cells. We plotted results for our model and for the PB model, which uses the LR formulation of  $I_{Na}$  dynamics. For comparison, we also added experimental CV data. Because no experimental data on human CVR are available, guinea pig CV data measured by Girouard et al. (19) were used. It can be seen that the CVR of our model agrees much better with experimental data; it declines less steeply and over a much broader range of diastolic intervals than is the case with the LR  $I_{Na}$  formulation.

Essential for the shape of the CVR curve is the recovery of  $I_{Na}$ , which is mainly determined by the recovery time constant of the slow inactivation gate  $j$ . Slowing down the dynamics of the  $j$  gate in the LR  $I_{Na}$  formulation makes CVR less steep and similar to that of our model (6). Note, however, that our CVR curve was not obtained by rescaling of a time constant but is based on our  $\tau_j$  formulation, which fits experimental data on human  $I_{Na}$ .

### Spiral Waves

The 2D simulations were performed on a  $600 \times 600$  square lattice of epicardial ventricular cells with  $\Delta x = 200 \mu\text{m}$ . Spiral waves were initiated with the S1-S2 stimulation protocol described in MATERIALS AND METHODS. The results of these computations are shown in Fig. 12. Figure 12A shows a typical spiral wave pattern after an initial period of spiral formation and stabilization (at 1.38 s after the S2 stimulus). The average period of the spiral wave is  $264.71 \pm 10.49$  ms, with an average APD of  $217.36 \pm 9.19$  ms and an average diastolic interval of  $47.21 \pm 6.13$  ms. The spiral wave meanders with a typical tip trajectory shown in Fig. 12B; the size of the core is  $\sim 3$  cm; the rotation type is similar to the “Z” core (see Fig. 12C) described by Fast et al. (15) and Efimov et al. (12), which combines regions of fast rotation of the tip (see Fig. 12C, A-B-C and D-E-F), typical of a circular core, with regions of laminar motion (see Fig. 12C, C-D) typical of a linear core.

Figure 13A shows an ECG recorded during spiral wave rotation. The ECG is similar to ECGs recorded during ventricular tachycardia. Figure 13, B and C, show recordings of membrane voltage in a point far away from the spiral core (star in Fig. 12A) and close to the spiral core (circle in Fig. 12B), respectively. Note the regular AP pattern in the point far from the core and the irregular pattern recorded close to the spiral core.

Similar results were obtained for simulations of sheets of endocardial and M cells. Wave patterns, tip trajectories, and ECG and membrane potential recordings were very similar (data not shown), the only real difference being the period of spiral wave rotation, which is  $264.23 \pm 10.37$  ms for endocardial and  $285.60 \pm 6.70$  ms for M cell tissue.

### DISCUSSION

In this paper we propose a model for human ventricular tissue. An important feature of our model is that all major ionic currents are fitted to recent data on human ventricular myocytes and expression experiments of human cardiac channels. This results in several important differences between our and previous models, the most important of which are the follow-

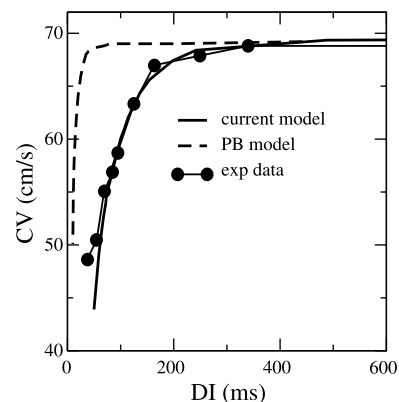
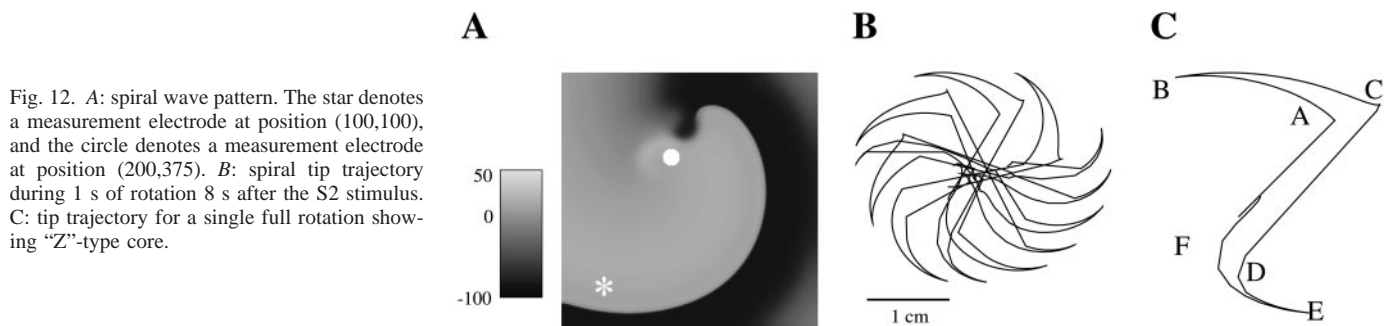


Fig. 11. Model conduction velocity restitution (CVR) curves for both the current model and the PB model obtained by pacing 1 end of a cable of a length of 400 cells with the dynamic restitution protocol. For comparison, experimental guinea pig CVR data measured by Girouard et al. (19) are added. The experimental data are rescaled by a factor of 0.92 to get the same maximum CV level as measured in human tissue.





ing: slower recovery dynamics of the fast sodium current, leading to a more gradual CVR that agrees better with available experimental data; differentiated formulations for epicardial and endocardial transient outward current, allowing the modeling of these different cell types; and an L-type calcium current with a fast, dominant, and stable calcium inactivation and slow voltage inactivation dynamics. In Table 3 the most important differences between the major ionic currents in our model and the LR, PB, and CRN models are summarized together with their electrophysiological consequences. In addition, conductance parameters used for these currents in our model and the other models are compared.

Our model reproduces three different cell types: endocardial, epicardial, and M cells with different characteristic action potential morphologies and rate dependencies. The APDR of

our model closely matches experimentally obtained APDR curves. In addition, the CVR of our model resembles experimentally obtained CVR curves, which are currently only available for animal cardiac tissue, much closer than CVR curves generated with models using the Luo-Rudy  $I_{Na}$  formulation. Both APDR and CVR are very important determinants for the stability of reentrant arrhythmias. Our calcium dynamics formulation is of a complexity comparable to that of the LR, PB, and CRN models and allows us to simulate a realistic calcium transient and a typical positive human contraction staircase.

The feasibility of spatial simulations is demonstrated with a simulation of a reentrant spiral wave in a 2D sheet of epicardial tissue. The period of spiral wave rotation is 254 ms, vs. 304 ms in the reduced PB model (3), because of the shorter APD in our model. The spiral wave tip trajectory is somewhat different from the linear tip trajectory found by Bernus et al. (3), because of the larger horizontal parts of the Z-type core. Another difference is that in the model by Bernus et al. (3) the core pattern has a cross section of  $\sim 5$  cm, whereas in our model the core pattern has a cross section of  $\sim 3$  cm, again because of the shorter APD in our model.

#### Limitations

A limitation of our model is that differences in APD and rate dependence between M cells and epicardial and endocardial cells in our model are smaller than the experimentally observed differences. This is because of the limited current knowledge of basic electrophysiological differences between M cells and the other cell types causing these differences. If these differences are further characterized, they can be easily incorporated in our model in terms of different current densities and/or dynamics for M cells, similar to what already has been done for  $I_{Ks}$  density differences.

We put considerable effort in obtaining, evaluating, rescaling to physiological conditions, and fitting of experimental data to get a model closely resembling true human ventricular cells. However, limitations are unavoidable because of the limited availability of data, the extensive variability among experimental data, the considerable variation in experimental conditions, and the potentially deleterious effects of cell isolation procedures used in voltage-clamp experiments.

There were no data available on  $I_{CaL}$  activation time constants, so formulations from another model based on animal experiments had to be used. The precise nature of calcium-mediated inactivation of the L-type calcium current is unknown. We used a simple description with a constant-valued time constant and a dependence on intracellular calcium only,

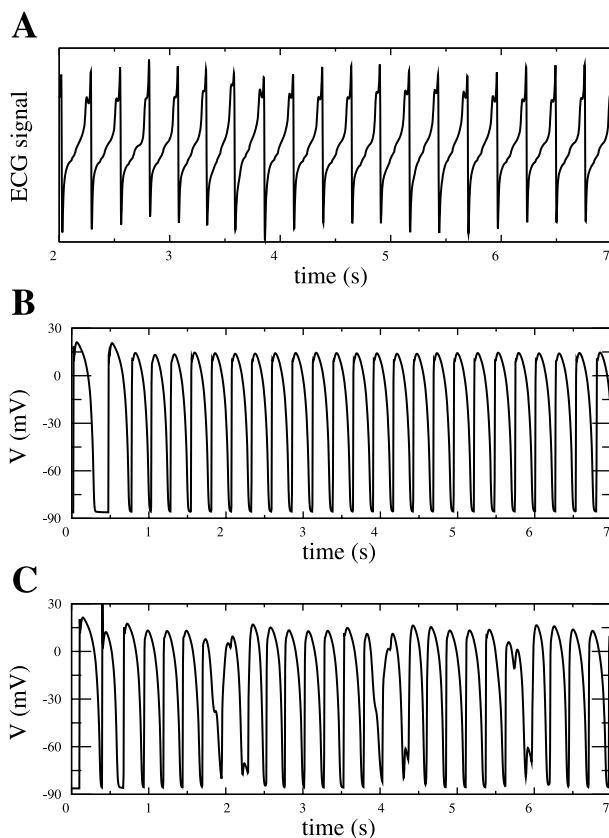


Fig. 13. A: ECG recorded during the spiral wave activity shown in Fig. 12A. B and C: membrane potential (V) recorded at point (100,100) (B) and point (200,375) (C) during 7 s after the application of S1. Point (100,100) corresponds to the star, and point (200,375) corresponds to the circle in Fig. 12A.

Table 3. Summary of most important differences in major currents between our model and original LR phase 2, PB, and CRN models and electrophysiological properties for which they are relevant

Current	Our Model	LR Model	PB Model	CRN Model
$I_{Na}$	Slow $\tau_j$ recovery from inactivation More gradual CV restitution	Faster $\tau_j$ recovery from inactivation Steep CV restitution	Same as in LR model	Same as in LR model
$G_{Na}$	14.838 nS/pF	16 nS/pF	16 nS/pF	7.8 nS/pF
$I_{CaL}$	Typical $\tau_f$ shape Slow $f$ gate inactivation Switchlike $f_{Ca}$ , large calcium inactivation Calcium-dominated inactivation GHK current model	Atypical $\tau_f$ shape Fast $f$ gate inactivation $f_{Ca}$ gradually declining Voltage-dominated inactivation GHK current model	Similar to LR model	Atypical $\tau_f$ shape Slow $f$ gate inactivation $f_{Ca}$ gradually declining Calcium-dominated inactivation Linear current model
$G_{CaL}$	$1.75^{-4} \text{ cm}^3 \cdot \mu\text{F}^{-1} \cdot \text{s}^{-1}$	$5.4^{-4} \text{ cm}^3 \cdot \mu\text{F}^{-1} \cdot \text{s}^{-1}$	Linear current model 0.064 nS/pF	Linear current model 0.1238 nS/pF
$I_{to}$	Different $G_{to}$ and recovery from inactivation dynamics for epicardial and endocardial cells	No $I_{to}$ current	Only epicardial $I_{to}$	Only epicardial $I_{to}$
$G_{to}$	0.294 nS/pF (epi), 0.073 nS/pF (endo)		0.3 nS/pF	0.1652 nS/pF
$I_{Ks}$	Slower activation and faster inactivation	No $I_{Ks}$ current	Faster activation and slower inactivation	Similar to PB model
$G_{Ks}$	0.245 nS/pF (epi/endo), 0.062 nS/pF (M cell)		0.02 nS/pF	0.129 nS/pF
$I_{Kr}$	Time-dependent inactivation gate Initial peak of current during AP	No $I_{Kr}$ current	Immediate inactivation gate No initial peak	Similar to PB model
$G_{Kr}$	0.096 nS/pF		0.015 nS/pF	0.0294 nS/pF

LR, Luo-Rudy; PB, Priebe-Beuckelman; CRN, Courtemanche and coworkers; GHK, Goldman-Hodgkin-Katz.

although data suggest that extracellular calcium also plays a role in inactivation (60). Finally, no data were available on the nature of calcium dynamics under high frequencies. We assumed calcium dynamics to stay stable under high frequencies. In addition, we assumed CICR to depend in a saturating manner on sarcoplasmic reticulum calcium content.

There is no agreement of experimental data on steady-state inactivation of  $I_{Na}$ . Some researchers give a value of  $-85$  mV for the voltage of half-inactivation (44, 55, 64), whereas others give a value of around  $-65$  mV (30, 40, 58). Rather than making a compromise, we decided to base our steady-state inactivation curves on data from Nagatomo et al. (44) because we also used their data for steady-state activation and time constants and wanted to maintain consistency.

Experiments are often performed at different temperatures. This is especially true for  $I_{Na}$  voltage-clamp experiments, where the temperature is usually below the physiological temperature to slow dynamics and limit current size. We derived a single  $Q_{10}$  factor and used this to rescale all  $I_{Na}$  time constants to  $37^\circ$ . Because it is not clear how steady-state curves change with temperature, we performed a linear extrapolation of the half-(in)activation voltages and slopes.

Experiments are also performed in the presence of different combinations of pharmacological agents used to suppress other currents. It is known that some of these chemicals have an impact on the dynamics of the measured current, e.g.,  $\text{Cd}^{2+}$  used to block L-type calcium current is known to influence steady-state curves of  $I_{to}$  current. We corrected experimental steady-state curves of  $I_{to}$  for the presence of  $\text{Cd}^{2+}$  by shifting them 10 mV in the positive direction.

To perform single-cell voltage-clamp experiments, cells must be isolated. These isolation procedures can have profound effects on the density of particular currents. A clear example of this are the  $I_{Ks}$  and  $I_{Kr}$  currents.  $I_{Ks}$  and  $I_{Kr}$  current densities found during voltage-clamp experiments are in sharp contrast with the clear relevance of these currents for action potential duration and restitution and the different behavior of M cells. We therefore decided to apply current densities for  $I_{Ks}$  and  $I_{Kr}$

that are substantially larger than experimentally measured densities and that allow us to realistically simulate the consequences of  $I_{Kr}$  block and the behavior of M cells.

In conclusion, we propose a new model for human ventricular epicardial, endocardial, and M cells based on ionic currents measured in human ventricular cells or measured in expression experiments using human cardiac channels. The model reproduces a number of experimental observations, ranging from voltage-clamp current traces and  $I$ - $V$  curves, to AP morphology, as well as APD and CV restitution curves and the contraction staircase. Because of its relative computational simplicity, the model is suitable for application in large-scale spatial simulations, which are necessary for investigating the dynamics of reentrant arrhythmias. The latter is illustrated with the simulation of a reentrant spiral wave in a 2D sheet of epicardial ventricular tissue.

## APPENDIX

### Reversal Potentials

$$E_X = \frac{RT}{zF} \log \frac{X_o}{X_i} \quad \text{for } X = \text{Na}^+, \text{K}^+, \text{Ca}^{2+} \quad (25)$$

$$E_{Ks} = \frac{RT}{F} \log \frac{K_o + p_{KNa} \text{Na}_o}{K_i + p_{KNa} \text{Na}_i} \quad (26)$$

### Fast $\text{Na}^+$ Current

$$I_{Na} = G_{Na} m^3 h j (V - E_{Na}) \quad (27)$$

$$m_\infty = \frac{1}{[1 + e^{(-56.86 - V)/9.03}]^2} \quad (28)$$

$$\alpha_m = \frac{1}{1 + e^{(-60 - V)/5}} \quad (29)$$

$$\beta_m = \frac{0.1}{1 + e^{(V+35)/5}} + \frac{0.1}{1 + e^{(V-50)/200}} \quad (30)$$

$$\tau_m = \alpha_m \beta_m \quad (31)$$

$$h_{\infty} = \frac{1}{[1 + e^{(V+71.55)/7.43}]^2} \quad (32)$$

$$\alpha_h = 0 \quad \text{if } V \geq -40 \quad (33)$$

$$\alpha_h = 0.057e^{-(V+80)/6.8} \quad \text{otherwise}$$

$$\beta_h = \frac{0.77}{0.13[1 + e^{-(V+10.66)/11.1}]} \quad \text{if } V \geq -40 \quad (34)$$

$$\beta_h = 2.7e^{0.079V} + 3.1 \times 10^5 e^{0.3485V} \quad \text{otherwise}$$

$$\tau_h = \frac{1}{\alpha_h + \beta_h} \quad (35)$$

$$j_{\infty} = \frac{1}{[1 + e^{(V+71.55)/7.43}]^2} \quad (36)$$

$$\alpha_j = 0 \quad \text{if } V \geq -40 \quad (37)$$

$$\alpha_j = \frac{\left( \frac{-2.5428 \times 10^4 e^{0.2444V} - 6.948}{\times 10^{-6} e^{-0.04391V}} \right) (V + 37.78)}{1 + e^{0.311(V+79.23)}} \quad \text{otherwise}$$

$$\beta_j = \frac{0.6e^{0.057V}}{1 + e^{-0.1(V+32)}} \quad \text{if } V \geq -40 \quad (38)$$

$$\beta_j = \frac{0.02424e^{-0.01052V}}{1 + e^{-0.1378(V+40.14)}} \quad \text{otherwise}$$

$$\tau_j = \frac{1}{\alpha_j + \beta_j} \quad (39)$$

#### L-type $\text{Ca}^{2+}$ Current

$$I_{\text{CaL}} = G_{\text{CaL}} d f_{\text{CaL}}^4 \frac{VF^2 \text{Ca}_i e^{2VF/RT} - 0.341 \text{Ca}_o}{RT e^{2VF/RT} - 1} \quad (40)$$

$$d_{\infty} = \frac{1}{1 + e^{(-5-V)/7.5}} \quad (41)$$

$$\alpha_d = \frac{1.4}{1 + e^{(-35-V)/13}} + 0.25 \quad (42)$$

$$\beta_d = \frac{1.4}{1 + e^{(V+5)/5}} \quad (43)$$

$$\gamma_d = \frac{1}{1 + e^{(50-V)/20}} \quad (44)$$

$$\tau_d = \alpha_d \beta_d + \gamma_d \quad (45)$$

$$f_{\infty} = \frac{1}{1 + e^{(V+20)/7}} \quad (46)$$

$$\tau_f = 1125e^{-(V+27)^2/240} + \frac{165}{1 + e^{(25-V)/10}} + 80 \quad (47)$$

$$\alpha_{f_{\text{Ca}}} = \frac{1}{1 + (\text{Ca}_i/0.000325)^8} \quad (48)$$

$$\beta_{f_{\text{Ca}}} = \frac{0.1}{1 + e^{(\text{Ca}_i - 0.0005)/0.0001}} \quad (49)$$

$$\gamma_{f_{\text{Ca}}} = \frac{0.2}{1 + e^{(\text{Ca}_i - 0.00075)/0.0008}} \quad (50)$$

$$f_{\text{Ca}\infty} = \frac{\alpha_{f_{\text{Ca}}} + \beta_{f_{\text{Ca}}} + \gamma_{f_{\text{Ca}}} + 0.23}{1.46} \quad (51)$$

$$\tau_{f_{\text{Ca}}} = 2 \text{ ms} \quad (52)$$

$$\frac{df_{\text{Ca}}}{dt} = k \frac{f_{\text{Ca}\infty} - f_{\text{Ca}}}{\tau_{f_{\text{Ca}}}} \quad (53)$$

$$k = 0 \quad \text{if } f_{\text{Ca}\infty} > f_{\text{Ca}} \quad \text{and } V > -60 \text{ mV} \quad (54)$$

$$k = 1 \quad \text{otherwise}$$

#### Transient Outward Current

$$I_{\text{to}} = G_{\text{to}} r_s (V - E_K) \quad (55)$$

For all cell types

$$r_{\infty} = \frac{1}{1 + e^{(20-V)/6}} \quad (56)$$

$$\tau_r = 9.5e^{-(V+40)^2/1800} + 0.8 \quad (57)$$

For epicardial and M cells

$$s_{\infty} = \frac{1}{1 + e^{(V+20)/5}} \quad (58)$$

$$\tau_s = 85e^{-(V+45)^2/320} + \frac{5}{1 + e^{(V-20)/5}} + 3 \quad (59)$$

For endocardial cells

$$s_{\infty} = \frac{1}{1 + e^{(V+28)/5}} \quad (60)$$

$$\tau_s = 1,000e^{-(V+67)^2/1,000} + 8 \quad (61)$$

#### Slow Delayed Rectifier Current

$$I_{\text{Ks}} = G_{\text{Ks}} x_s^2 (V - E_{\text{Ks}}) \quad (62)$$

$$x_{s\infty} = \frac{1}{1 + e^{(-5-V)/14}} \quad (63)$$

$$\alpha_{xs} = \frac{1,100}{\sqrt{1 + e^{(-10-V)/6}}} \quad (64)$$

$$\beta_{xs} = \frac{1}{1 + e^{(V-60)/20}} \quad (65)$$

$$\tau_{xs} = \alpha_{xs} \beta_{xs} \quad (66)$$

#### Rapid Delayed Rectifier Current

$$I_{\text{Kr}} = G_{\text{Kr}} \sqrt{\frac{\text{K}_o}{5.4}} x_{r1} x_{r2} (V - E_K) \quad (67)$$

$$x_{r1\infty} = \frac{1}{1 + e^{(-26-V)/7}} \quad (68)$$

$$\alpha_{xr1} = \frac{450}{1 + e^{(-45-V)/10}} \quad (69)$$

$$\beta_{xr1} = \frac{6}{1 + e^{(V+30)/11.5}} \quad (70)$$

$$\tau_{xr1} = \alpha_{xr1} \beta_{xr1} \quad (71)$$

$$x_{r2\infty} = \frac{1}{1 + e^{(V+88)/24}} \quad (72)$$

$$\alpha_{xr2} = \frac{3}{1 + e^{(-60-V)/20}} \quad (73)$$

$$\beta_{xr2} = \frac{1.12}{1 + e^{(V-60)/20}} \quad (74)$$



$$\tau_{xr2} = \alpha_{xr2} \beta_{xr2} \quad (75)$$

Inward Rectifier  $K^+$  Current

$$I_{K1} = G_{K1} \sqrt{\frac{K_o}{5.4}} x_{K1\infty} (V - E_K) \quad (76)$$

$$\alpha_{K1} = \frac{0.1}{1 + e^{0.06(V - E_K - 200)}} \quad (77)$$

$$\beta_{K1} = \frac{3e^{0.0002(V - E_K + 100)} + e^{0.1(V - E_K - 10)}}{1 + e^{-0.5(V - E_K)}} \quad (78)$$

$$x_{K1\infty} = \frac{\alpha_{K1}}{\alpha_{K1} + \beta_{K1}} \quad (79)$$

$Na^+/Ca^{2+}$  Exchanger Current

$$I_{NaCa} = k_{NaCa} \frac{e^{\gamma VF/RT} Na_i^3 Ca_o - e^{(\gamma-1)VF/RT} Na_o^3 Ca_i \alpha}{(K_{mNa}^3 + Na_o^3)(K_{mCa} + Ca_o)(1 + k_{sat} e^{(\gamma-1)VF/RT})} \quad (80)$$

$Na^+/K^+$  Pump Current

$$I_{NaK} = P_{NaK} \frac{K_o Na_i}{(K_o + K_{mK})(Na_i + K_{mNa})(1 + 0.1245e^{-0.1VF/RT} + 0.0353e^{-VF/RT})} \quad (81)$$

$I_{pCa}$

$$I_{pCa} = G_{pCa} \frac{Ca_i}{K_{pCa} + Ca_i} \quad (82)$$

$I_{pK}$

$$I_{pK} = G_{pK} \frac{V - E_K}{1 + e^{(25-V)/5.98}} \quad (83)$$

Background Currents

$$I_{bNa} = G_{bNa} (V - E_{Na}) \quad (84)$$

$$I_{bCa} = G_{bCa} (V - E_{Ca}) \quad (85)$$

Calcium Dynamics

$$I_{leak} = V_{leak} (Ca_{sr} - Ca_i) \quad (86)$$

$$I_{up} = \frac{V_{maxup}}{1 + K_{up}^2 / Ca_i^2} \quad (87)$$

$$I_{rel} = \left( a_{rel} \frac{Ca_{sr}^2}{b_{rel}^2 + Ca_{sr}^2} + c_{rel} \right) dg \quad (88)$$

$$g_{\infty} = \frac{1}{1 + Ca_i^6 / 0.00035^6} \quad \text{if } Ca_i \leq 0.00035 \quad (89)$$

$$g_{\infty} = \frac{1}{1 + Ca_i^{16} / 0.00035^{16}} \quad \text{otherwise} \quad (90)$$

$$\tau_g = 2 \text{ ms} \quad (91)$$

$$\frac{dg}{dt} = k \frac{g_{\infty} - g}{\tau_g} \quad (92)$$

$$k = 0 \quad \text{if } g_{\infty} > g \quad \text{and } V > -60 \text{ mV}$$

$$k = 1 \quad \text{otherwise}$$

$$Ca_{ibufc} = \frac{Ca_i \times Buf_c}{Ca_i + K_{bufc}} \quad (93)$$

$$\frac{dCa_{itotal}}{dt} = - \frac{I_{CaL} + I_{bCa} + I_{pCa} - 2I_{NaCa}}{2V_C F} + I_{leak} - I_{up} + I_{rel} \quad (94)$$

$$Ca_{srbufsr} = \frac{Ca_{sr} \times Buf_{sr}}{Ca_{sr} + K_{bufsr}} \quad (95)$$

$$\frac{dCa_{srtotal}}{dt} = \frac{V_C}{V_{SR}} (-I_{leak} + I_{up} - I_{rel}) \quad (96)$$

Sodium and Potassium Dynamics

$$\frac{dNa_i}{dt} = - \frac{I_{Na} + I_{bNa} + 3I_{NaK} + 3I_{NaCa}}{V_C F} \quad (97)$$

$$\frac{dK_i}{dt} = - \frac{I_{K1} + I_{to} + I_{Kr} + I_{Ks} - 2I_{NaK} + I_{pK} + I_{stim} - I_{ax}}{V_C F} \quad (98)$$

## ACKNOWLEDGMENTS

We are thankful to Dr. O. Bernus and Dr. R. Wilders for valuable discussions.

This work was initiated during a visit of A. V. Panfilov at the Isaac Newton Institute for Mathematical Sciences in 2001.

## GRANTS

This work was funded by the Netherlands Organization for Scientific Research (NWO) through Grant 620061351 of the Research Council for Physical Sciences (EW) (to K. H. W. J. ten Tusscher), the Netherlands National Computer Facilities Foundation (NCF) through Grant SG-095, the British Heart Foundation, the British Medical Research Council, the Wellcome Trust, and Physiome Sciences (to D. Noble and P. J. Noble)

## REFERENCES

1. Beeler GW and Reuter H. Reconstruction of the action potential of ventricular myocardial fibers. *J Physiol* 268: 177–210, 1977.
2. Benitah J, Bailly P, D'Agrosa M, Da Ponte J, Delgado C, and Lorente P. Slow inward current in single cells isolated from adult human ventricles. *Pflügers Arch* 421: 176–187, 1992.
3. Bernus O, Wilders R, Zemlin CW, Verschelde H, and Panfilov AV. A computationally efficient electrophysiological model of human ventricular cells. *Am J Physiol Heart Circ Physiol* 282: H2296–H2308, 2002.
4. Beuckelmann DJ, Nabauer M, and Erdmann E. Characteristics of calcium-current in isolated human ventricular myocytes from patients with terminal heart failure. *J Mol Cell Cardiol* 23: 929–937, 1991.
5. Boyett MR and Fedida D. A computer simulation of the effect of heart rate on ion concentrations in the heart. *J Theor Biol* 132: 15–27, 1988.
6. Cao J, Qu Z, Kim Y, Wu T, Garfinkel A, Weiss JN, Karagueuzian HS, and Chen P. Spatiotemporal heterogeneity in the induction of ventricular fibrillation by rapid pacing, importance of cardiac restitution properties. *Circ Res* 84: 1318–1331, 1999.
7. Chudin E, Goldhaber J, Garfinkel J, Weiss A, and Kogan B. Intracellular  $Ca^{2+}$  dynamics and the stability of ventricular tachycardia. *Biophys J* 77: 2930–2941, 1999.
8. Courtemanche M, Ramirez RJ, and Nattel S. Ionic mechanisms underlying human atrial action potential properties: insights from a mathematical model. *Am J Physiol Heart Circ Physiol* 275: H301–H321, 1998.
9. Drouin E, Charpentier F, Gauthier C, Laurent K, and Le Marec H. Electrophysiologic characteristics of cells spanning the left ventricular wall of human heart: evidence for the presence of M cells. *J Am Coll Cardiol* 26: 185–192, 1995.
10. Drouin E, Lande G, and Charpentier F. Amiodarone reduces transmural heterogeneity of repolarization in the human heart. *J Am Coll Cardiol* 32: 1063–1067, 1998.
11. Ebihara L and Johnson EA. Fast sodium current in cardiac muscle, a quantitative description. *Biophys J* 32: 779–790, 1980.
12. Efimov IR, Krinsky VI, and Jalife J. Dynamics of rotating vortices in the Beeler-Reuter model of cardiac tissue. *Chaos Solitons Fractals* 5: 513–526, 1995.
13. Endresen LP, Hall K, Høye JS, and Myrheim J. A theory for the membrane potential of living cells. *Eur Biophys J* 29: 90–103, 2000.
14. Endresen LP and Skarland N. Limit cycle oscillations in pacemaker cells. *IEEE Trans Biomed Eng* 47: 1134–1137, 2000.

15. Fast VG, Efimov IR, and Krinsky VI. Transition from circular to linear cores in excitable media. *Phys Lett A* 151: 157–161, 1990.
16. Fenton F and Karma A. Vortex dynamics in three-dimensional continuous myocardium with fiber rotation: filament instability and fibrillation. *Chaos* 8: 20–47, 1998.
17. Garfinkel A, Kim YH, Voroshilovsky O, Qu Z, Kil JR, Lee MH, Karagueuzian HS, Weiss JN, and Chen PS. Preventing ventricular fibrillation by flattening cardiac restitution. *Proc Natl Acad Sci USA* 97: 6061–6066, 2000.
18. Gintant GA. Characterization and functional consequences of delayed rectifier current transient in ventricular repolarization. *Am J Physiol Heart Circ Physiol* 278: H806–H817, 2000.
19. Girouard SD, Pastore JM, Laurita KR, Greogry KW, and Rosenbaum DS. Optical mapping in a new guinea pig model of ventricular tachycardia reveals mechanisms for multiple wavelengths in a single reentrant circuit. *Circulation* 93: 603–613, 1996.
20. Grantham CJ and Cannell MB.  $\text{Ca}^{2+}$  influx during the cardiac action potential in guinea pig ventricular myocytes. *Circ Res* 79: 194–200, 1996.
21. Greenstein JL and Winslow RL. An integrative model of the cardiac ventricular myocyte incorporating local control of  $\text{Ca}^{2+}$  release. *Biophys J* 83: 2918–2945, 2002.
22. Greenstein JL, Wu R, Po S, Tomaselli GF, and Winslow RL. Role of the calcium-independent transient outward current  $I_{\text{to1}}$  in shaping action potential morphology and duration. *Circ Res* 87: 1026–1033, 2000.
23. Hodgkin AL and Huxley AF. A quantitative description of membrane current and its application to conduction and excitation in nerve. *J Physiol* 117: 500–544, 1952.
24. Hund TJ, Kucera JP, Otani NF, and Rudy Y. Ionic charge conservation and long-term steady state in the Luo-Rudy dynamic cell model. *Biophys J* 81: 3324–3331, 2001.
25. Iost N, Virag L, Opincariu M, Szecsi J, Varro A, and Papp JG. Delayed rectifier potassium current in undiseased human ventricular myocytes. *Cardiovasc Res* 40: 508–515, 1998.
26. Beuckelmann DJ, Nabauer M, and Erdmann E. Intracellular calcium handling in isolated ventricular myocytes from patients with terminal heart failure. *Circulation* 94: 992–1002, 1992.
27. Janvier NC and Boyett MR. The role of the Na-Ca exchange current in the cardiac action potential. *Cardiovasc Res* 32: 69–84, 1996.
28. Johnson JP, Mullins FM, and Bennet PB. Human Ether-a-go-go-related gene  $\text{K}^{+}$  channel gating probed with extracellular  $\text{Ca}^{2+}$ , evidence for two distinct voltage sensors. *J Gen Physiol* 113: 565–580, 1999.
29. Jongsma HJ and Wilders R. Gap junctions in cardiovascular disease. *Circ Res* 86: 1193–1197, 2000.
30. Kambouris NG, Nuss HB, Johns DC, Marban E, Tomaselli GF, and Balser JR. A revised view of cardiac sodium channel “blockade” in the long-QT syndrome. *J Clin Invest* 105: 1133–1140, 2000.
31. Karma A. Electrical alternans and spiral wave breakup in cardiac tissue. *Chaos* 4: 461–472, 1994.
32. Koller ML, Riccio ML, and Gilmour RF Jr. Dynamic restitution of action potential duration during electrical alternans and ventricular fibrillation. *Am J Physiol Heart Circ Physiol* 275: H1635–H1642, 1998.
33. Koumi S, Backer CL, and Arentzen CE. Characterization of inwardly rectifying  $\text{K}^{+}$  channel in human cardiac myocytes. *Circulation* 92: 164–174, 1995.
34. Li G, Feng J, Yue L, Carrier M, and Nattel S. Evidence for two components of delayed rectifier  $\text{K}^{+}$  current in human ventricular myocytes. *Circ Res* 78: 689–696, 1996.
35. Li G and Nattel S. Properties of human atrial  $I_{\text{Ca}}$  at physiological temperatures and relevance to action potential. *Am J Physiol Heart Circ Physiol* 272: H227–H235, 1997.
36. Li GR, Feng J, Yue L, and Carrier M. Transmural heterogeneity of action potentials and  $I_{\text{to1}}$  in myocytes isolated from the human right ventricle. *Am J Physiol Heart Circ Physiol* 275: H369–H377, 1998.
37. Luo C and Rudy Y. A model of the ventricular cardiac action potential, depolarization, repolarization, and their interaction. *Circ Res* 68: 1501–1526, 1991.
38. Luo C and Rudy Y. A dynamic model of the cardiac ventricular action potential. I. simulations of ionic currents and concentration changes. *Circ Res* 74: 1071–1096, 1994.
39. Magyar J, Szentandrássy N, Banyasz T, Fulop L, Varro A, and Nanasi PP. Effects of thymol on calcium and potassium currents in canine and human ventricular cardiomyocytes. *Br J Pharmacol* 136: 330–338, 2002.
40. Makita N, Shirai N, Wang DW, Sasaki K, George AL, Kanno M, and Kitabatake A. Cardiac  $\text{Na}^{+}$  channel dysfunction in Brugada syndrome is aggravated by  $\beta_1$ -subunit. *Circulation* 101: 54–60, 2000.
41. Mewes T and Ravens U. L-type calcium currents of human myocytes from ventricle of non-failing and failing hearts and atrium. *J Mol Cell Cardiol* 26: 1307–1320, 1994.
42. Morgan JM, Cunningham D, and Rowland E. Dispersion of monophasic action potential duration: demonstrable in humans after premature ventricular extrastimulation but not in steady state. *J Am Coll Cardiol* 19: 1244–1253, 1992.
43. Nabauer M, Beuckelmann DJ, Überfuhr P, and Steinbeck G. Regional differences in current density and rate-dependent properties of the transient outward current in subepicardial and subendocardial myocytes of human left ventricle. *Circulation* 93: 168–177, 1996.
44. Nagatomo T, Fan Z, Ye B, Tonkovich GS, January CT, Kyle JW, and Makielski JC. Temperature dependence of early and late currents in human cardiac wild-type and long Q-T  $\Delta\text{KPQ Na}^{+}$  channels. *Am J Physiol Heart Circ Physiol* 275: H2016–H2024, 1998.
45. Noble D, Varghese A, Kohl P, and Noble P. Improved guinea-pig ventricular cell model incorporating a diadic space,  $I_{\text{Kr}}$  and  $I_{\text{Ks}}$ , and length- and tension-dependent processes. *Can J Cardiol* 14: 123–134, 1998.
46. Pelzmann B, Schaffer P, Bernhart E, Lang P, Machler H, Rigler B, and Koilb B. L-type calcium current in human ventricular myocytes at a physiological temperature from children with tetralogy of Fallot. *Cardiovasc Res* 38: 424–432, 1998.
47. Perea Y, Demolombe S, Baro I, Drouin E, Charpentier F, and Escande D. Differential expression of KvLQT1 isoforms across the human ventricular wall. *Am J Physiol Heart Circ Physiol* 278: H1908–H1915, 2000.
48. Pieske B, Maier LS, Bers DM, and Hasenfuss G.  $\text{Ca}^{2+}$  handling and sarcoplasmic reticulum  $\text{Ca}^{2+}$  content in isolated failing and non-failing human myocardium. *Circ Res* 85: 38–46, 1999.
49. Pieske B, Maier LS, Piacentino V, Weisser J, Hasenfuss G, and Houser S. Rate dependence of ( $\text{Na}^{+}$ ), and contractility in nonfailing and failing human myocardium. *Circ Res* 106: 447–453, 2002.
50. Plonsey R and Barr RC. *Bioelectricity*. New York: Plenum, 1989.
51. Priebe L and Beuckelmann DJ. Simulation study of cellular electric properties in heart failure. *Circ Res* 82: 1206–1223, 1998.
52. Qu Z, Weiss JN, and Garfinkel A. Cardiac electrical restitution properties and stability of reentrant spiral waves: a simulation study. *Am J Physiol Heart Circ Physiol* 276: H269–H283, 1999.
53. Rice JJ, Jafri MS, and Winslow RL. Modeling gain and gradedness of  $\text{Ca}^{2+}$  release in the functional unit of the cardiac diadic space. *Biophys J* 77: 1871–1884, 1999.
54. Rush S and Larsen H. A practical algorithm for solving dynamic membrane equations. *IEEE Trans Biomed Eng* 25: 389–392, 1978.
55. Sakakibara Y, Wasserstrom JA, Furukawa T, Jia H, Arentzen CE, Hartz RS, and Singe DH. Characterization of the sodium current in single human atrial myocytes. *Circ Res* 71: 535–546, 1992.
56. Sakmann BFAS, Spindler AJ, Bryant SM, Linz KW, and Noble D. Distribution of a persistent sodium current across the ventricular wall in guinea pig. *Circ Res* 87: 910–914, 2000.
57. Schmidt U, Hajjar RJ, Helm PA, Kim CS, Doye AA, and Gwathmey JK. Contribution of abnormal sarcoplasmic reticulum ATPase activity to systolic and diastolic dysfunction in human heart failure. *J Mol Cell Cardiol* 30: 1929–1937, 1998.
58. Schneider M, Proebstle T, Hombach V, Hannekum A, and Rudel R. Characterization of the sodium currents in isolated human cardiocytes. *Pflügers Arch* 428: 84–90, 1994.
59. Smith PL and Yellen G. Fast and slow voltage sensor movements in HERG potassium channels. *J Gen Physiol* 119: 275–293, 2002.
60. Sun H, Leblanc N, and Nattel S. Mechanisms of inactivation of L-type calcium channels in human atrial myocytes. *Am J Physiol Heart Circ Physiol* 272: H1625–H1635, 1997.
61. Taggart P, Sutton PMI, Ophof T, Coronel R, Trimlett R, Pugsley W, and Kallis P. Inhomogeneous transmural conduction during early ischemia in patients with coronary artery disease. *J Mol Cell Cardiol* 32: 621–639, 2000.
62. Virag L, Iost N, Opincariu M, Szolnoky J, Szecsi J, Bogats G, Szenohradszky P, Varro A, and Papp JP. The slow component of the delayed rectifier potassium current in undiseased human ventricular myocytes. *Cardiovasc Res* 49: 790–797, 2001.
63. Viswanathan PC, Bezzina CR, George AL, Roden DM, Wilde AAM, and Balser JR. Gating-dependent mechanism for flecainide action in SCN5A-linked arrhythmia syndromes. *Circulation* 104: 1200–1205, 2001.

64. Wan X, Chen S, Sadeghpour A, Wang Q, and Kirsch GE. Accelerated inactivation in a mutant  $\text{Na}^+$  channel associated with idiopathic ventricular fibrillation. *Am J Physiol Heart Circ Physiol* 280: H354–H360, 2001.
65. Wang DW, Makita N, Kirabatake A, Balser JR, and George AL. Enhanced  $\text{Na}^+$  channel intermediate inactivation in Brugada syndrome. *Circ Res* 87: e37–e43, 2000.
66. Wang Z, Fermini B, and Nattel S. Rapid and slow components of delayed rectifier current in human atrial myocytes. *Cardiovasc Res* 28: 1540–1546, 1994.
67. Watanabe MA, Fenton FH, Evans SJ, Hastings HM, and Karma A. Mechanisms for discordant alternans. *J Cardiovasc Electrophysiol* 12: 196–206, 2001.
68. Wettwer E, Amos GJ, Posival H, and Ravens U. Transient outward current in human ventricular myocytes of subepicardial and subendocardial origin. *Circ Res* 75: 473–482, 1994.
69. Xie F, Qu Z, Garfinkel A, and Weiss JN. Effects of simulated ischemia on spiral wave stability. *Am J Physiol Heart Circ Physiol* 280: H1667–H1673, 2001.
70. Yue L, Feng J, Li GR, and Nattel S. Transient outward and delayed rectifier currents in canine atrium: properties and role of isolation methods. *Am J Physiol Heart Circ Physiol* 270: H2157–H2168, 1996.
71. Zeng J, Laurita KR, Rosenbaum DS, and Rudy Y. Two components of the delayed rectifier  $\text{K}^+$  current in ventricular myocytes of the guinea pig type. Theoretical formulation and their role in repolarization. *Circ Res* 77: 140–152, 1995.
72. Zhou Z, Gong Q, Ye B, Fan Z, Makielski JC, Robertson GA, and January CT. Properties of HERG channels stably expressed in HEK 293 cells studied at physiological temperatures. *Biophys J* 74: 230–241, 1997.
73. Zygmunt AC, Eddlestone GT, Thomas GP, Nesterenko VV, and Antzelevitch C. Larger late sodium conductance in M cells contributes to electrical heterogeneity in canine ventricle. *Am J Physiol Heart Circ Physiol* 281: H689–H697, 2001.
74. Zygmunt AC, Goodrow RJ, and Antzelevitch C.  $I_{\text{NaCa}}$  contributes to electrical heterogeneity within the canine ventricle. *Am J Physiol Heart Circ Physiol* 278: H1671–H1678, 2000.

